

The Globular Cluster System of NGC 1399. I. A Wide-field Photometric Study

³

B. Dirsch ¹, T. Richtler ¹, D. Geisler ¹, J.C. Forte ², L.P. Bassino ², W.P. Gieren ¹

bdirsch@cepheid.cfm.udc.cl

ABSTRACT

We present a photometric investigation of the globular cluster population of NGC 1399, the central galaxy in the Fornax cluster, in Washington C and Kron R filters within a field of $36' \times 36'$, corresponding to about 200×200 kpc at the Fornax distance. This is the largest area around this galaxy ever studied with CCD photometry. The cluster system of NGC 1399 is found to extend further than 100 kpc away from the galaxy. The color distribution exhibits a pronounced bimodality. Within a radial distance of about 55 kpc, the red clusters are more strongly concentrated to the center than the blue clusters. At larger radii, the surface density profiles of the clusters are indistinguishable and match well the distribution of the galaxy light. Over the entire radial distance range, the surface brightness profile of NGC 1399 can be very well fitted by a power law with an exponent of -1.85 and a core radius of $3.3''$. No steepening of the luminosity profile can be detected at large radii. We suggest that the power law profile of NGC 1399 results from the galaxy being embedded in a large dark matter halo, which prevents the stellar density profile from steepening outwards. The cluster system contains 6450 ± 700 clusters and the specific frequency is found to be 5.1 ± 1.2 in the V band. While NGC 1399 shows a pronounced color gradient the nearby comparison galaxy NGC 1404 does not show such a gradient. Using simple assumptions about the underlying population that formed during the same star formation event as the globular clusters, we present a model in which we use radially changing local specific frequencies for the red and blue subpopulations to fit the observations. We find that within $7'$ the required specific frequency of the blue clusters alone is a factor of approximately 3 larger than that of the red ones. Outside this radius however, both populations have a same high local specific frequency of around 8 and 13 (blue and red clusters, respectively).

Subject headings: galaxies: individual (NGC 1399, NGC 1404) — galaxies: elliptical

¹Universidad de Concepción, Departamento de Física, Casilla 160-C, Concepción, Chile

²Facultad de Ciencias Astronómicas y Geofísicas, Universidad Nacional de La Plata, Paseo del Bosque S/N, 1900-La Plata, Argentina

³Based partly on observations collected at the European Southern Observatory, Cerro Paranal, Chile; ESO program 66.B-0393.

and lenticular, cD — galaxies: clusters: general — galaxies: photometry — galaxies: halos

1. Introduction

One of the central and challenging topics in the context of the structure and evolution of early-type galaxies is the investigation of their globular clusters systems (GCSs), how they formed, and what they might tell us about the formation of their host galaxies (for recent reviews on the subject, see Ashman & Zepf (1998), Elmegreen (1999), van den Bergh (2000), Harris (2001)).

It has now emerged from numerous studies (e.g. Kundu & Whitmore (2001a), Kundu & Whitmore (2001b), Larsen et al.(2001), Gebhardt & Kissler-Patig (1999), Geisler et al. (1996), Whitmore et al. (1995), Zepf & Ashman (1993)) that GCSs of early-type galaxies are by no means homogeneous populations, but exhibit substructure in terms of metallicity, kinematics and spatial distribution. The formation of massive clusters does not occur in isolation, but probably even needs to be accompanied by strong star forming activity in general. This is apparent in ongoing merger events (see the list in Harris (2001)) but also in the case of “normal” spiral galaxies (Larsen & Richtler (1999), (2000)). Therefore, the presence of GCs must be indicative of a corresponding field population with similar ages and metallicities and thus GCs might be considered as tracers of this field population, which otherwise is unaccessible due to the low surface brightness of galaxy halos and/or because it is mixed up with other populations.

It might then be possible to trace back the population composition of an elliptical galaxy, the distinct metallicities and spatial distributions of the subcomponents, and compare these properties to what is expected if, for example, the elliptical galaxy is a result of a merger (or multiple merger) of disk galaxies (Bekki et al. (2002)). However, the relation of a GCS and its components to the field components can be complicated. Even if the efficiency of cluster formation per unit mass had a universal value, as argued by McLaughlin ((1999)), it does not mean that one can infer directly the luminosity of the underlying field population from the number of globular clusters because generally the fate of the gas is unknown.

A promising target to gain better insight into the connection between the relation of cluster subpopulations to the underlying field population is NGC 1399, the central galaxy of the Fornax cluster. It has long been known to possess a large number of globular clusters (Dawe & Dickens (1976)) out to large radii (Hanes & Harris (1986), Harris & Hanes (1987)). Photographic studies of NGC 1399 showed that its luminosity profile cannot be described by a de Vaucouleurs profile but by a power-law (Schombert (1986), Killeen & Bicknell (1988), Caon et al. (1994)). Whether NGC 1399 is a cD galaxy or not depends on the applied definition, which in turn differs from author to author. For example, Bridges et al. (1991) classify it as a cD, while Schombert (1986) does not include it in his list of cD galaxies. The spatial distribution of galaxy light and globular clusters have been compared by Bridges et al. ((1991)) and Wagner et al. ((1991)) who performed the first

CCD studies of the GCS of NGC 1399. Except for the very inner regions, both studies found the surface density profile of the clusters to agree well with the galaxy light. Wagner et al. and Bridges et al. also obtained the first color information of the GCS using the B and V bands. While Wagner et al. could not see a color gradient, Bridges et al. detected a shift of 0.2 mag to the blue between 0.5' and 3'. The latter authors moreover derived a turn-over magnitude of $V=23.8$ and a distance of 18.5 Mpc, which still is in very good agreement with modern values (Richtler et al. (2000)). The specific frequency (which is the total number of globular clusters normalized to the host galaxy's luminosity, Harris & Van den Bergh ((1981))), derived by Harris & Hanes ((1987)), Bridges et al. ((1991)) and Wagner et al. ((1991)) was unusually large for an elliptical galaxy (16 ± 4), a property which is shared with other central galaxies in galaxy clusters (e.g. Harris (2001)).

The next contribution came from the Washington system: Ostrov et al. ((1993)) measured Washington colors of NGC 1399 globular clusters and also detected the color gradient reported earlier. They also mentioned a "multimodality" in the metallicity distribution, indicating that the GCS could be composed of different populations with distinct properties. Kissler-Patig et al. ((1997)) also noted the broad V-I color distribution of the NGC 1399 clusters in comparison with other Fornax ellipticals and a high specific frequency, but could not confirm the color gradient seen by Ostrov et al. ((1993)) and Bridges et al. ((1991)).

An improved photometric analysis in the Washington system (Ostrov et al. (1998)) showed that the color distribution of the clusters was rather "bi-modal" than "multi-modal". In this work, a rather low specific frequency of only 5.6 was derived.

The open questions are still: How far does the NGC 1399 GCS extend? What substructure can be identified and how does it relate to the host galaxy? Does the population structure change in the outer parts? How does the cluster distribution compare to the stellar distribution? What significance does the quoting of a general specific frequency have, if the GCS is substructured?

From the photometric side, progress can only be expected if a much larger field is investigated than has been done in the past. With the advent of the new MOSAIC cameras, we now have the opportunity to do this. Moreover, the excellent metallicity resolution of the Washington photometric system enables us to reconsider the metallicity distribution based on much better number statistics than in previous studies.

This paper is part of a larger effort to study NGC 1399 and its cluster population. The second paper in this series by Richtler et al. ((2002)) (Paper II) will use spectroscopic observations of globular clusters for a dynamical study of NGC 1399.

2. Observation & Reduction

2.1. The Data and Basic Reduction

Data from 5 observing runs are contributing to the present photometric study. The main data set consists of Washington wide-field images of NGC 1399 (plus a background field) taken with the MOSAIC camera mounted at the prime focus of the CTIO 4m Blanco telescope. Additionally, three sub-fields were observed at the VLT (FORS2) in V and I. The location of the MOSAIC field around NGC 1399 and the VLT fields are shown in Fig. 1 as overlays on a DSS image.

We used the Kron-Cousins R and Washington C filters, although the genuine Washington system uses T1 instead of R. However, Geisler (1996) has shown that the Kron-Cousins R filter is more efficient than T1, due to its larger bandwidth and higher throughput, and that R and T1 magnitudes are closely related, with only a very small color term and zero-point difference ($R - T1 \approx -0.02$). The MOSAIC wide-field camera images a field of $36' \times 36'$, at a pixel scale of $0.27''/\text{pixel}$. The first three observing runs were performed in the 8 channel read-out mode; for the last one (November 2001) the 16 channel mode was available. Further information on the MOSAIC camera can be found in the MOSAIC homepage ⁴.

During the first run (December 1999), we observed one MOSAIC field centered near NGC 1399 (see Fig. 1) in the C filter, while the R band images were kindly obtained by D.Zurek and M.Shara.

In the second run (December 2000), we observed a background field 3.5° north-east of NGC 1399 (RA= $3^h48'$ Dec= $-32^\circ32'$) in C and R, as well as Washington standard fields.

In the third run (November 2001), we observed adjacent fields to NGC 1399 that overlap with the central field. We also observed standard fields under photometric conditions. This run was used for the photometric calibration of the presented Washington data.

In addition to the MOSAIC data, we analyzed three fields ($6.8' \times 6.8'$) near NGC 1399 for which 5 min exposures in V and I were taken with VLT/FORS2 in December 2000, in the course of a campaign aimed at measuring radial velocities of globular clusters around NGC 1399 (Richtler et al. (2001)).

In Tab. 10 we summarize the relevant information on the different observing runs.

The MOSAIC data were reduced using the *mscred* package within IRAF. In particular this software is able to correct for the variable pixel scale across the CCD which would cause otherwise a 4% variability of the brightness of stellar-like objects from the center to the corners. The flatfielding resulted in images that had remaining sensitivity variations $\leq 1.5\%$. In particular Chip #4 and Chip #5 showed discernible remaining flatfield structure (but within the given deviation).

To facilitate the search for point sources on the MOSAIC images model light profiles of

⁴<http://www.noao.edu/kpno/mosaic/mosaic.html>

NGC 1399 as well as of the neighboring galaxies NGC 1404 and NGC 1387 were subtracted. This was done using a median filter with an inner radius of $9.5''$ and an outer radius of $11''$. This size is large enough for not altering the point source photometry which has been verified with artificial star tests described later on.

2.2. Identification of Point Sources

We used SExtractor (Bertin & Arnouts (1996)) and DAOPHOT II for image classification and photometry, respectively. Our extensive tests showed that each program was optimized for these respective tasks. To distinguish between point sources and extended objects, we compared the SExtractor stellarity indices for objects found both on the MOSAIC and the VLT images. With the aid of the superior seeing on the VLT images, we determined 0.4 as a lower limit for the SExtractor classifier on the MOSAIC images.

Using this classification, the comparison with the VLT fields revealed that $(90 \pm 5)\%$ of the point sources found in the MOSAIC fields were correctly classified as point sources. Only 1.2 ± 0.1 galaxies arcmin^{-2} have been erroneously classified as point sources in the MOSAIC images. With less a strict selection criterion one could lower the number of lost point sources. However, this would come at the expense of additional contamination by background galaxies. Since we are interested in the GCS at large radii, i.e. at low surface densities, we rather prefer a lower completeness over an increased contamination by galaxies.

We retained 10453 point sources while 13600 resolved objects were discarded. The brightest non-saturated objects have $R \approx 18$ (slightly depending on the individual MOSAIC chip).

For further study we chose a faint magnitude cut-off, depending on color. The limit also accounts for the fact that the background field is not as deep as the NGC 1399 field. We therefore defined this cut-off by the completeness limit of the background field and regarded only objects brighter than this limit (see Fig. 3).

2.3. Photometric Calibration

Standard fields for the photometric calibration have been observed during the November 2001 run. In each of the 3 nights, we observed 4-5 fields, each containing about 10 standard stars from the list of Geisler ((1996)), with a large coverage of airmasses (typically from 1.0 to 1.9). It was possible to use a single transformation for all three nights, since the coefficients derived for the different nights were indistinguishable within the errors.

We derived the following relations between instrumental and standard magnitudes:

$$T1 = R_{\text{inst}} + (0.72 \pm 0.01) - (0.08 \pm 0.01)X_R$$

$$\begin{aligned}
 & + (0.021 \pm 0.004)(C - T1) \\
 C = & C_{\text{inst}} - (0.06 \pm 0.02) - (0.30 \pm 0.01)X_C \\
 & + (0.074 \pm 0.004)(C - T1)
 \end{aligned}$$

The standard deviation of the difference between our calibrated and tabulated magnitudes is 0.018 mag in T1 and 0.027 mag in C (see Fig. 2).

To calibrate the NGC 1399 field we identified isolated stars which have been observed on three overlapping fields during the November 2001 run. These stars were used to determine the zero points, while the color terms were adopted from the November 2001 run. The scatter between the zero points determined from individual stars is 0.03 mag and most probably due to flat field uncertainties.

The final uncertainties of the zero points are 0.03 mag and 0.04 mag for R and C, respectively. This results in a calibration uncertainty in C-T1 of 0.05 mag (the uncertainty in the color term can be neglected).

Ostrov et al. ((1998)) also obtained Washington photometry for a smaller field centered on NGC 1399. We used their Fig. 6 and Fig. 10 to obtain the color and luminosity distribution of their objects. In Fig. 10 we compare the color distribution of the same subfield, and in Fig. 9 the luminosity functions are compared. These figures show the good agreement between the two photometric data sets.

The VLT data in V and I have been calibrated using the zero points, airmass coefficients and color terms published on the ESO Web page for the corresponding night ⁵. We used the same zero point for all fields despite the fact that the gain is different for all four amplifiers, since we divided by a normalized flatfield and thus we had to average the gain as well (in the high gain mode). The ESO calibration for the I filter includes a color term $I_0 \propto I_{\text{inst}} - 0.07(V - R)$. Because we had no VLT observations in the R band, we used a subset of clusters for which we had VLT (V,I) and (MOSAIC) R observations and found the the following relation between (V-I) and (V-R) colors: $(V-R) = -(0.10 \pm 0.04) + (0.47 \pm 0.04)(V-I)$, with a scatter of $\sigma_{V-R} = 0.04$ mag. This relation is used for the photometric calibration where no R observations were available. This procedure introduces an error of 0.04 mag in the final magnitudes as one can judge from the scatter of the relation. For Milky Way GCs the following can be obtained with the data assembled in the Mc Master catalogue (Harris (1996)): $(V-R) = -(0.01 \pm 0.01) + (0.49 \pm 0.01)(V-I)$. Thus while the slope of the relation is the same, the V-R color is either 0.09 mag bluer in NGC 1399 than in the Milky Way or the V-I color is systematically 0.09 mag redder. The reason for this difference is unclear. We found for the three nights (the subscripts denote the nights):

⁵<http://www.eso.org/observing/dfo/quality/FORS/qc/zeropoints/zeropoints.html>

$$\begin{aligned}
 V_1 &= v_{\text{inst}} + 28.057 + (0.74) - 0.16X_V \\
 I_1 &= i_{\text{inst}} + 27.284 + (0.74) - 0.16X_I - 0.07(V_1 - R_1) \\
 V_2 &= v_{\text{inst}} + 28.048 + (0.74) - 0.16X_V \\
 I_2 &= i_{\text{inst}} + 27.263 + (0.74) - 0.16X_I - 0.07(V_2 - R_2) \\
 V_3 &= v_{\text{inst}} + 28.038 + (0.74) - 0.16X_V \\
 I_3 &= i_{\text{inst}} + 27.261 + (0.74) - 0.16X_I - 0.07(V_3 - R_3)
 \end{aligned}$$

We note the term due to the conversion from ADUs to electrons (0.74) separately to facilitate the comparison with the zero points given in the ESO Web page.

For the reddening towards NGC 1399 we adopted, according to Schlegel et al. ((1998)), $E_{B-V} = 0.013$. Using $E_{C-T1} = 1.97 E_{B-V}$ (Harris & Canterna (1977)) we have to correct C-T1 by 0.026 mag. For the comparison field the foreground reddening is negligible: $E_{B-V} = 0.002$.

The color magnitude diagrams for the point sources in the MOSAIC images are plotted in Fig. 3. The combined color-magnitude diagram for the three VLT fields is shown in Fig. 5.

2.4. Photometric Completeness

The globular cluster luminosity function (GCLF) will be derived from the VLT images only, so the photometric incompleteness as a function of apparent magnitude of the MOSAIC images is not of much interest to our current study. However, it is interesting to know the global incompleteness, and how many objects, being resolved in the VLT images, were falsely classified as point sources in the MOSAIC images. We found that within our magnitude range, $(41 \pm 3)\%$ of the cluster candidates visible on the VLT frames were detected on the MOSAIC images. 0.5 objects/arcmin² which are resolved in the VLT images have been classified as point sources in the MOSAIC images (objects brighter than the employed faint magnitude limit). This is a reassuringly small number.

Dithering to fill the gaps between the eight individual CCD chips was done only for the C images. Therefore one has to consider the spatial incompleteness due to the gaps between the MOSAIC CCDs in the R images, saturated galaxy centers and some bright stars west of NGC 1399 which account for a spatial incompleteness of $\approx 4\%$ in the MOSAIC data.

Experiments with artificial stars were performed in order to check on whether a magnitude-dependent difference between input and output magnitude is observed among the point sources. This was not the case, and thus the size of the median filter we used to model and subtract the galaxy light, is justified. Additionally, we found that for point sources more distant from NGC 1399 than 1.6', no radially varying completeness has to be corrected for.

The completeness of the VLT fields has been determined with extensive artificial star tests. We

used *addstar* of the DAOPhot package under IRAF to add 5 times 2000 stars to each VLT image. The stellar PSF was the same as determined by the PSF fitting routine in the same package. The color and magnitude range encompassed the range of observed globular clusters. The resulting completeness as a function of V magnitude is shown in Fig. 6.

3. The Color Magnitude Diagram

We will now discuss the CMD presented in Fig. 3 and Fig. 5. The globular clusters show up nicely in Fig. 3 within the color range $1.1 < C - T1 < 2.3$. In its vast majority the cluster population belongs to NGC 1399, but the GCSs of NGC 1404 and NGC 1387 are also included. The combination of a large area, depth, and broad color baseline render this CMD unique among the available photometric data sets of cluster systems. The cluster population starts at about $T1=20$. Well visible is the blue "peak" in the color distribution, while the red clusters rather build a "shoulder" and do not distinctly peak at a certain color (see section 5 for a detailed discussion of the color distribution). The comparison with the background field (Fig. 4) shows how well it reproduces the shoulder starting at $C-T1 = 0$ and the red peak (stars) at $C-T1 = 3$.

The comparison between the VLT and the MOSAIC data also shows why the contamination of the cluster system by background galaxies is much lower for the filter combination C,R than for V,I, even if the seeing is considerably worse. The reason can be seen in Fig. 7. The main sources that contaminate the cluster sample in V & I are unresolved faint blue galaxies that have an UV excess and are thus bluer than cluster candidates in C-R while having the same V-I color. We confirm the galaxy nature of these (C-T1)-blue objects since they have a homogeneous distribution and are not concentrated towards NGC 1399 like the cluster candidates.

4. The Globular Cluster Luminosity Function

To derive the globular cluster luminosity function (GCLF) of the VLT data we selected clusters within a radial distance of $4.3'$ from the center of NGC 1399. As a background field we used the FORS2 image centered $13'$ away from NGC 1399. We are aware of the fact that this "background field" still contains a considerable number of clusters apart from background objects, which deteriorates the statistics, but should not alter the location of the turn-over magnitude (TOM).

The luminosity function is also plotted as kernel filtered density distributions. We followed here the approach described by Merritt & Tremblay ((1994)) and used an adaptive Epanechnikov kernel. The scaling in Fig. 8 is number of clusters per 0.2 magnitude. In the following, all distributions using this nonparametric estimation are based on the Epanechnikov kernel. For the fitting we use both, filtered data and the histograms to ensure that the results do not depend on the representation.

We fitted a Gaussian to the distributions for different limiting magnitudes (always brighter

than the 50% completeness) and found an average $\sigma = 1.30 \pm 0.12$ and $m_{\text{TO}} = 24.0 \pm 0.1$. However, a correlation between σ and TOM exist these fits which is caused by the fact that our observations do not extend far enough beyond the TOM. It is therefore advisable to keep the width fixed and to fit only the TOM. With a $\sigma = 1.2, 1.3, 1.4$, which are used for elliptical galaxies (Ashman & Zepf (1998)), we find a TOM of $23.98 \pm 0.11, 24.02 \pm 0.09, 24.05 \pm 0.12$. We choose the same final TOM of $m_{\text{TO}} = 24.0 \pm 0.1$.

With the knowledge of the TOM we calculate that the fraction of all clusters which are found in the area covered by the VLT data is $85\% \pm 4\%$.

The background-subtracted luminosity functions of the MOSAIC cluster candidates from $2'$ to $16'$ (excluding $2'$ around NGC 1404) are shown in Fig.9. The luminosity distributions are consistent with the assumed distance modulus of $m - M = 31.4$ and a width of the Gaussian luminosity function of 1.2.

This TOM together with the known completeness of the VLT data can be used to determine the completeness of the MOSAIC fields. Since $41\% \pm 3\%$ of the VLT candidates were found on the MOSAIC images (see above) the absolute completeness is $36\% \pm 5\%$ for the MOSAIC images.

An alternative approach to find the completeness is to use the luminosity function of the MOSAIC clusters directly: using a TOM of $T1 = 23.3$ and a width of $\sigma = 1.2$ (Forte et al. (2001)) we find a completeness of $41 \pm 2\%$. We adopt a final completeness of $34\% \pm 5\%$, taking into account a spatial incompleteness due to the undithered gaps of 4%.

The GCLF is frequently used as a distance indicator for early-type galaxies due to its universal peak luminosity (e.g. Harris (1991), Harris (2001), Ashman et al. (1995), Kundu & Whitmore (2001a), Larsen et al. (2001)). However, due to the uncertainty of the VLT calibration we do not use the obtained TOM for more than the above presented completeness calculations for which the absolute calibration is not critical.

In the following we use a distance to NGC 1399 of $m - M = 31.4 \pm 0.2$ consistent with SBF distances (Tonry et al. (2001), Liu et al. (2002)), however only marginally consistent with the result of Grillmair et al. ((1999)), from the GCLF technique.

5. Color Distribution of the Clusters

In the CMD of all point sources around NGC 1399 (Fig. 3) the GC candidates stand out strikingly. A blue peak at $C-T1 = 1.3$ followed by a broad distribution towards redder colors is prominently visible. In the following, we define GC candidates by the magnitude interval $20 < T1 < 23$ and the color interval $0.8 < C - T1 < 2.3$.

In Fig. 10 we plot the background subtracted color distribution for the cluster candidates for the entire sample and in three different ranges in radial distance. It is apparent that the color distribution is radially dependent: at larger radii the relative contribution of the red clusters is much smaller than at lower radii. This already shows that the blue clusters exhibit a shallower density profile than the red clusters, as has already been found by several authors. However, it is also apparent that this might not hold for larger radii: the two outer distributions (the two lower panels in Fig. 10) look quite similar and are statistically not distinguishable. The distributions plotted in Fig. 10 are tabulated in Table 2. The two peaks in the innermost sample are at $C - T1 = 1.32 \pm 0.05$ and 1.79 ± 0.03 , respectively.

Since so far only a few GCS have been studied in the Washington system, our possibilities for comparison with other work are quite limited.

As mentioned above, NGC 1399 has already been studied by Ostrov et al. ((1998)) who found a bimodal distribution with peaks at $C-T1 \approx 1.4$ and $C-T1 \approx 1.8$, agreeing with our values for the inner region. This is also shown in the upper right panel of Fig. 10.

6. Radial Distribution of the Clusters

The area we cover is the largest ever observed for the NGC 1399 GCS. However, the innermost region is unaccessible due to the brightness of the galaxy and the saturated parts of the images. Therefore we combined our data with HST observations by Forbes et al. ((1998)) in order to include also the inner part of NGC 1399 in our study. We extrapolated all three samples (HST, VLT, Mosaic) to the entire luminosity function with the parameters given in section 3. In Fig. 12 the resulting surface densities of GCs are plotted for the three samples. The HST results are in excellent agreement with our data at overlapping radii, demonstrating the validity of our completeness calculations. A fit which satisfactorily reproduces the surface densities of the total number of clusters after completeness correction is:

$$n(r) = 200 \cdot (1 + (r/1')^2)^{-0.8} [\text{arcmin}^{-2}] \quad (1)$$

In the following, we focus on the MOSAIC sample. From the color histograms in Fig. 10 one can immediately see that the red clusters are more centrally concentrated than the blue ones. Guided by Fig. 10, we define the color limit between red and blue clusters to be $C-T1 = 1.55$, which is the

minimum seen in the clearly bimodal color distribution seen in the upper right panel of Fig. 10. We can now quantify the radial surface density distributions displayed in Fig.13, which show the density profiles for both populations. Because the inner region, where a core is visible, is excluded, we can describe the density profiles by pure power-laws.

Out to a galactocentric radius of about $7'$, the blue clusters show a distinctly shallower slope than the red clusters. This has already been found in earlier studies of NGC 1399 (e.g. Forbes et al. (1998), Ostrov et al. (1998)) as well as in other galaxies, NGC 4636 being the most striking example (Kissler et al. (1994)).

The region beyond $7'$ has as yet been unexplored and indeed we see an interesting change. The distribution of the red population is well represented by a single power-law over the full radius interval between $2'$ and $20'$, but the blue population shows a change from a shallow profile in the inner region to a steeper profile in the outer region. Here, two power-laws are more appropriate. For the blue clusters, the profiles are proportional to $r^{-0.8 \pm 0.17}$ and $r^{-1.71 \pm 0.21}$ (for $1.5' < r < 7'$ and $7' < r < 21'$, respectively). For the red population, we find the profile $\propto r^{-1.64 \pm 0.10}$. Thus we cannot see any significant difference in the slope between red and blue cluster distributions beyond $7'$ of radial distance. This can also be quantified with a K-S test for which we selected only clusters brighter than $R=22.5$ to minimize the effect of the background. This test results in a 48% probability that the red and blue clusters at large radii have a different radial distribution. This probability should be considered as upper limit, since we did not correct for the background contamination which affects the red and blue color range differently. This indicates again that the distribution of red and blue clusters is consistent with being the same.

One might recognize that the slopes fitted to the MOSAIC data at large radii are shallower than the fit to all GCs over the whole radial range presented above. This is also apparent from Fig. 12, which suggests that the assumption of a uniform power-law over the whole galactocentric distance range might not be adequate. At larger radii – where the investigation is restricted to the MOSAIC data – the slope is shallower.

To provide an independent check, we derived the radial profiles for the red and blue subsamples between $1'$ and $8'$ also from the VLT data. We only used cluster candidates brighter than $V=22$ mag to avoid the background contamination coming from the faint blue galaxies, which in $V-I$ cannot be distinguished from cluster candidates (see Fig. 7). Moreover, the VLT fields only cover approximately 11% of the MOSAIC field and thus the statistics are poorer and the errors larger. In spite of this, the resulting density distributions of metal-poor ($0.7 < (V - I) < 0.95$) and metal-rich clusters ($1.05 < (V - I) < 1.2$) agree very well with the results obtained with the Washington observations: The exponents are -1.0 ± 0.13 and -1.5 ± 0.18 for the blue and the red populations, respectively. However, a difference emerges for the blue population at small radii. If we only consider the blue clusters within $5'$, we obtain an exponent of -0.5 ± 0.09 compared to -1.2 ± 0.2 (based on 4 points) outside this radius. This indicates that the assumption of two power-laws describing the metal-poor population is probably too simple.

Besides NGC 1399, NGC 4472 – the brightest galaxy in the Virgo cluster – is the only elliptical galaxy where the GCS has been studied with wide-field CCD photometry (Rhode & Zepf (2001)). Due to its similar distance (17 Mpc) and similar size the results for this galaxy can readily compared with ours. In particular the radial distributions of red and blue clusters found by Rhode & Zepf ((2001)) is very similar to our results for NGC 1399. This includes the mentioned "out-leveling" of the number ratio of red versus blue clusters at large radii, i.e. the same radial decline of red and blue clusters is indicated.

6.1. The Brightest Clusters

In Fig. 11 we show the color distribution for three different brightness bins. It is striking that for the brightest clusters, shown in the uppermost panel, the color distribution differs largely from the fainter samples seen (this is already apparent in the CMD): compared to the fainter sample more intermediate colored ($C - T1 \approx 1.55$) are present. A Kolmogorov-Smirnov test (K-S test) resulted in only a 5% probability that the bright sample has the same color distribution as the fainter one ($R=21-22$). Ostrov et al. ((1998)) suggested that the brightest clusters might have a unimodal distribution, however their lower number of objects did not permit a clear statement. In the faintest magnitude bin, the red peak is shifted towards the blue with respect to the intermediate bin. This, however, may be easily explained by the inclined completeness line that does affect only this bin. These bright clusters are as concentrated as the red clusters and do not have the shallow distribution of the blue ones: a K-S test results in a 1% probability that the bright ones are not distributed than the red ones and a 95% probability that they have a different distribution than the blue ones.

7. The Galaxy Light Profile

It is now of interest to compare the surface density profile of the GCS with that of the galaxy light and to search for any color gradient, which would indicate a correspondence between the GCS and the galaxy population itself.

Previous photographic work covering a similarly large field has been carried out by Schombert ((1986); V-band) and Caon et al.((1994); B-band). The resulting profiles are plotted in Fig. 14. Beyond a radius of $5'$ they begin to diverge in the sense that the V profile gets brighter than the B profile. Besides the fact that this "color gradient" has the very unexpected sense of getting redder, it also reaches the unreasonably high value of almost 2 mag at $14'$. We conclude that either V or B, or both, are not reliable at faint surface brightness values. We therefore tried to derive the light profile from our images as well.

We measured the brightness around all point sources within an annulus between $8''$ and $11''$ on the point source-subtracted C and R images. We defined this brightness to be the mode of the

distribution of pixel intensities after a 5% clipping of the brightest peaks. Without the σ clipping the scatter would have been significantly larger.

Care has to be taken due to the use of eight different chips and corresponding differences in the sensitivities that are left after flatfielding. To account for these differences we shifted the zero points of individual chips to a common mean value by adjusting the sky brightness in adjacent fields. The resulting correction factors are of the order of 0.3% of the background level in the R image and in the order of 1% in the C images. Since the R images are deeper we used them to trace the galaxy light to large radii, whereas the C data has been used to search for a color gradient at smaller radii. We excluded regions with bright stars, other galaxies and obvious flatfield structure (chip #4, chip #5 and upper part of chip #8). The inner 2' are saturated.

The most difficult part in determining the galaxy luminosity profile is the correct determination of the sky background: a tiny 0.5% deviation in the sky level has already a profound effect on the galaxy light distribution as shown in Fig. 14 for the T1 profile. In the upper panel the luminosity profile is given for different sky values; these sky levels are indicated in a linear intensity scale in the lower panel, where the x-axis is enlarged. Individual measurements are plotted as dots. If we would have reached the true sky background, profile **b** would be appropriate and our resulting luminosity profile would look nearly identical to that of Caon et al. ((1994)). However, the measurements suggest that the galaxy light has not yet leveled out. On the other hand profile **a** can be excluded, since the observed background is clearly lower than the one belonging to this profile. The profile by Schombert et al. can be reproduced (profile **d**) when using the lowest background in the lower panel of Fig. 14, but such a low background is almost certainly excluded since in this case the galaxy would have a radial extension of approximately 500 kpc and hence it would be one of the largest galaxies known. As will be discussed later on, profile **c**, based on our preferred background also resembles well that of the GCs and thus we adopt it as our preferred profile. The difference with the B-profile of Caon et al. would still suggest a color which becomes redder with increasing distance, contrary to what we find (see below). Only profile **a** delivers a color gradient in the required sense, but this is not supported by our data.

From Fig. 14 it is also apparent that the profile becomes rather diffuse for radii smaller than approximately 6'. The reason for this is the non-negligible ellipticity of NGC 1399. The lower profile envelope belongs to the minor axis while the upper one belongs to the major axis. We determined an average decline only, but this poses no problem for the comparison with the cluster distribution, which has also been determined assuming a circular geometry. Moreover, the slope of a power-law is not altered by averaging over the ellipticity. We nevertheless used this information to derive the radial dependence of the ellipticity which is shown in the next section.

The C-profile reaches the background level already at 13' due to the shallower C-data and we determine the background by averaging the “profile” at larger radii.

Between 2.5' and 9' (where the effects of the background uncertainty are still tolerable) we fitted power-laws to the profile and obtained exponents of -1.85 ± 0.03 for the T1 profile and of

-1.21 ± 0.02 for the C profile, thus finding a clearly shallower C-profile. This holds for any sky background which deviates no more than 2% from our measured background, to which we assign an error of less than 1%. The color gradient in C-T1 is shown in the lower panel of Fig. 20 in Sec.7.2. The color gradient is also plotted as a smoothed curve, together with error limits that are estimated from the background uncertainties, in Fig. 21.

We see that the color gradient might level out to a constant value of C-T1 around 1.2 at $6'$, which is approximately the same radius beyond which the blue and red GCs start to show indistinguishable surface density profiles. This might be evidence that the behavior of the GCS is indeed reflected in the field star population. However, the mean color of the clusters at this radius is (linearly averaged) C-T1=1.47, and hence considerably redder than the galaxy color.

7.1. Covering the whole Radial Range

We are unable to determine the total magnitude of NGC 1399 because of the missing inner $2'$. However, we can proceed by taking this data from the literature. In Fig. 15 we plot the available luminosity profiles which were shifted onto our T1-magnitude scale using our T1-profile. We shifted Caon et al.’s and Schombert et al.’s data in the range between $1'$ and $1.5'$. In the innermost region a V-profile based on HST observations has been published by Lauer et al. (1995), which we used out to $12''$. In the range between $12''$ and $1.5'$, we used the B profile of Caon et al. (1994). For larger radii, we used our profile. Color gradients in B-R and V-R in the inner region are very small and should not introduce significant errors (e.g. Idiart et al. (2002)).

From this data we can construct a luminosity profile for NGC 1399 that covers 3 orders of magnitude in radius. In Tab. 10 we list this profile, together with the integrated T1 magnitude at selected radii.

A good fit to the surface brightness profile of NGC 1399 is:

$$T1(r) = 2.125 \log(1 + (r/0.055')^2) + 15.75. \quad (2)$$

The deviation from the fit is shown in Fig. 16, where we plot the difference between observed and fitted magnitude. Similarly to the globular cluster density profile, the fit to the light profile using the whole radial range also results in a profile being too steep at large radii (see Fig. 16). For these large radii, an exponent of 1.83 as derived above is more adequate. Integrating this profile, one obtains the total R-luminosity of NGC 1399: $M_R = -23.33$ (assuming a distance modulus of 31.4 and an absolute solar luminosity of $M_{R\odot} = 4.28$.).

If we adopt spherical geometry, one can derive the deprojected profile. Because we have the profile as an analytic expression, an easier way than to apply the deprojection formula is to adopt a power-law of the above form, use the projection formula and vary the parameters until the best

fit is found.

Using this procedure, the best fit we obtain is:

$$L(T1)[L_{\odot}/pc^3] = 101 \cdot (1 + r/221pc)^{-2.85}. \quad (3)$$

We also determined the ellipticity of NGC 1399. However, we did not try to fit a position angle to the rather noisy data, but estimated the position angle rather by eye inspection of the image. We used a fixed position angle of 90° . The position angle variation from 110° to 85° seen by Caon et al. ((1994)) is not critical since it occurs between $30''$ and $1.35'$, while our profile starts at $2'$. The resulting radial dependence of the ellipticity is shown in Fig. 17 together with Caon et al.'s values. The two measurements are in good agreement. The ellipticity of NGC 1399 is 0.1 between $2'$ and $4'$, then it rises to about 0.2 at $5'$. The further decline at larger radii is rather uncertain, since at these large radii our azimuthal coverage is not homogeneous due to the exclusion of areas with bright stars, other galaxies and obviously remaining flatfield structure.

In Fig. 18 we compare the integrated light profile with aperture measurements from the literature. This figure shows that our determination agrees well with the literature values, and that our data do not suggest any systematic zero point difference.

8. The Specific Frequency

The specific frequency is the number of globular clusters per unit luminosity scaled to a galaxy with an absolute luminosity of $M_V = -15$ mag ($S_V = N \cdot 10^{0.4(M_V - 15)}$).

In Fig. 12, the galaxy light profile is compared with the cluster density profile over nearly the whole observed radial range. Determining the specific frequency means integrating over both curves. In the inner part the galaxy light is more concentrated than the globular clusters, which reflects the fact that the core radius of the GCS is about 18 times larger than that of the field population. This also means that the specific frequency is not radially constant. We shall proceed in deriving first a global value, and then study the radial dependence of the specific frequency for both red and blue clusters.

8.1. The Global Specific Frequency

To derive the total number of clusters we have to account for the incompleteness with respect to the globular cluster luminosity function. In Sect. 2.4 we determined this to be $(35 \pm 5)\%$.

Within the radial range from $2'$ to $17'$ (excluding a radius of $2'$ around NGC 1404), we find 2600 ± 50 cluster candidates. Within the central $2'$ Forbes et al. ((1998)) found 700 clusters. From our background field we know that a cluster candidate sample brighter than $T1 = 23.5$ has a con-

tamination of 0.48 ± 0.02 objects/arcmin 2 . Accounting for this contamination and incompleteness, we find a total number of 6100 ± 770 clusters within 83 kpc (15').

Alternatively, we integrated the density profile derived in Sec. 7 and obtained a number of 6800 ± 950 clusters within 83 kpc. Within 10', this results in 5793 clusters. Averaging the results of both determinations we find the total number of clusters within 15' to be 6450 ± 700 . Our obtained number agrees well with what has been found for the cluster content within 10': Ostrov et al. ((1998)), Forbes et al. ((1998)), and Kissler-Patig et al. ((1997)) all quote ≈ 5700 clusters within 10'. In the inner part we have an excellent agreement with older studies, too: within 1.5' and 2.5' we determine a total number of 734 ± 114 clusters, while Ostrov et al. found 746 ± 80 , and within 2.5' and 4' we have 921 ± 140 whereas Ostrov et al. give 967 ± 100 .

With this total number of clusters, we find a global specific frequency of $S_R = 3.2 \pm 0.7$ using a total galaxy magnitude of $T1 = 8.08$ (Table 3) and $m-M = 31.4 \pm 0.2$. Since we cannot measure the galaxy light in the V band, we have to convert $T1$ into V magnitudes to be able to compare our value with the literature. Using a color of $V-R = 0.55$ (Mackie (1990)) we find a specific frequency of $S_V = 5.1 \pm 1.2$ within 15'.

Forbes et al. ((1998)) quoted a specific frequency of 11.5 ± 1 . They used an absolute magnitude of $M_V = -21.74$ (taken from Faber et al. (1989)), while we would use $T1 = 8.25$, which translates to $M_V = -22.59$ (see above) for the total luminosity (within 10'). Part of the difference comes from the different distance modulus adopted by Forbes et al. ($m-M = 31.2$). However, the major discrepancy is in the apparent magnitude: Faber et al. give the B_T , magnitude which is defined as the magnitude within the 25 mag/arcsec 2 isophote. Using a $B-R = 1.8$ value, we find that 25 mag/arcsec 2 corresponds to a radius of 3.8'. Within this radius we measure an approximate B luminosity (again assuming no B-R color gradient) of 10.4 mag, which is in reasonable agreement, considering all uncertainties to the Faber et al. value of $B = 10.55$. The same argument can also be applied to explain the high specific frequencies determined by Kissler-Patig et al. ((1997)), Wagner et al. ((1991)), and Bridges et al. ((1991)). This shows that one of the most important caveats in deriving the specific frequency is that the clusters and the galaxy light has to be measured within the same area, a fact that has already been pointed out by Ostrov et al. ((1998)) for the case of NGC 1399.

8.2. The Local Specific Frequency

Because of the existence of subpopulations in the GCS, it is useful to define a local specific frequency where the number of GCs is normalized to the brightness of the area in which they are counted.

The local specific frequency of the red, the blue and the total cluster sample for different radial bins is given in Tab.4 and displayed in Fig.19. Since the galaxy light profile in the R band matches well the radial distribution of the red cluster population within 11', its local specific

frequency remains nearly constant around $S_R = 3$. Outside of $11'$ small background uncertainties make a definite statement on the surface brightness profile difficult. However, using a reasonable background it is easy to find a galaxy profile that follows the red clusters also at these large radii. The blue cluster system, on the other hand, shows within $11'$ a slightly shallower profile and therefore its specific frequency with respect to the R band luminosity increases outwards proportional to $r^{0.8 \pm 0.2}$. However, the behavior at larger radii is uncertain as well.

9. Discussion

9.1. The Cluster Color Distribution

In general, there is little doubt that the color of a GC indicates its metallicity in an old elliptical galaxy like NGC 1399 (however, we cannot exclude that younger clusters are mixed in; Forbes et al. (2001b)). The GC color distribution has been the starting point for many investigations regarding the substructure of GCSs of elliptical galaxies. It has been found by many authors (e.g. Kundu & Whitmore (2001a), Forbes & Forte (2001a), Larsen et al. (2001), Gebhardt & Kissler-Patig (1999), see also the corresponding section in the book of Ashman and Zepf (1998)) that GCSs often exhibit two peaks in the color distribution, labeled as "bimodality". If bimodality is not obvious then frequently at least the existence of two peaks is statistically better supported than an unimodal color distribution. Usually, a linear transformation between color and metallicity without accounting to an intrinsic scatter around the mean color metallicity is applied (e.g. Harris et al. (2000), Kissler-Patig et al. (1997), Harris et al. (1991)). This means that a bimodal color distribution translates into a bimodal metallicity distribution which is assigned to two different populations. Because bimodal color distributions of clusters in ellipticals have been predicted by Ashman & Zepf (1992) in the context of a simple merger scenario, color bimodality has been interpreted supporting the formation of GCSs of elliptical host galaxies in merger events. However, despite the fact that a merger *can* produce a bimodal color distribution it is not clear whether a bimodal distribution *necessarily* implies a merger scenario, e.g. even in a monolithic collapse scenario a bimodal metallicity distribution (of stars) can be obtained: Samland et al. ((1997)) simulated the formation of a disk galaxy starting with a coherent gas cloud. They found that disk, halo and bulge stars have different metallicity distributions (their Fig.7). If one plots their Fig.7 in logarithmic metallicity bins a bi- or even multimodal metallicity distribution becomes apparent. They note "that a bimodal star formation or a pre-enrichment of the protogalactic cloud is not required by our model. The metallicity distributions for the different galactic regions result purely from the local star formation history, the large-scale gas flows, and the phase transitions by condensation and evaporation."

We also would like to call attention to the fact that the color-metallicity relation is non-linear, flattening out in the metal-poor regime (Harris & Harris (2002)). In conjunction with an intrinsic spread in the color-metallicity relation due to second parameters and photometric errors, this leads

to the circumstance that, starting from the bluest colors equidistant color intervals are projected onto progressively larger metallicity intervals, which decrease once the linear regime is reached. What this effect means for the interpretation in particular of the blue peak, is certainly worth to investigate, but beyond the scope of our paper.

The question whether the color distribution of a GCS depends on the host galaxy's properties is still unclear. Regarding the Washington system only few GCSs have been studied: Geisler et al. ((1996)) investigated the GCS of NGC 4472 and obtained $C - T1 \approx 1.3$ and $C - T1 \approx 1.8$ for the colors of the blue and red peak, respectively. The blue peak of NGC 1427, a low luminosity elliptical galaxy, also agrees with the blue peak of the NGC 1399 clusters ($C - T1 \approx 1.4$, Forte et al. (2001)). M 87 also has a GCS with a bimodal color distribution that peaks at $C - T1 \approx 1.25$, while the position of the red peak remains uncertain in the color histogram shown by Côté et al. (2001), which is based on still unpublished photometry. Two more GCSs for which Washington photometry have been obtained are those of NGC 3311 (Secker et al. (1995)) and NGC 3923 (Zepf et al. (1995)). Both galaxies (which have been observed during the same run) show abnormally red color distributions. However, Brodie et al. (2000) performed V-I photometry with HST in NGC 3311 and found a normal bimodal distribution with peaks at the expected colors. Since the Washington run was not photometric, one might conjecture that both NGC 3311 and NGC 3923 were subject to calibration uncertainties. Together with our results on NGC 1399 we conclude that at least the blue peaks have very similar colors in those GCSs of elliptical galaxies investigated so far with Washington photometry.

9.2. Interpreting the Radial Cluster Distribution

In Paper II, we will show that the blue and red clusters within $7'$ are also kinematically distinct: The red clusters have a velocity dispersion of 274 ± 15 km/s, while the blue clusters have 310 ± 10 km/s. This larger dispersion can well be accounted for in the framework of a spherically dynamical model due to the different surface density slopes. In other words, a higher/lower dispersion is dynamically equivalent to a shallower/steeper surface density profile in an isotropic equilibrium situation.

A distinction of two subpopulations on the basis of the color histogram alone bears a high degree of uncertainty. However, in light of the correlation between metallicity and density profile/kinematics, we find it justified to talk about two populations out to a radius of about $7'$. However, that does not necessarily imply the existence of two *distinct* populations, in the sense of different formation epochs or formation mechanisms. It may well be that there is a continuum of properties, over which our color sampling is simply taking an average. Going to larger galactocentric radii, the distinction between subpopulations becomes much less pronounced. The density profiles of blue and red clusters are more or less the same and the color distribution indicates a broad range of metallicities, even if two Gaussians are still a better representation than one Gaussian, but as we said above, we do not assign too much physical significance to that.

Despite the large field used we have not yet reached the background. The total extension of the GCS of NGC 1399 is hence not yet known. However, for GCs with a very large radii the question remains whether such clusters should be considered as belonging to NGC 1399 or as an "intergalactic GC population" (White (1987), West et al. (1995)). Bassino et al. ((2002)) used Washington observations around dwarf elliptical galaxies in the Fornax clusters to search for GCs at large radii. They found a GC candidate surface density of $0.25 \pm 0.08/\text{arcmin}^2$ and $0.12 \pm 0.06/\text{arcmin}^2$ at a radial distance of $40'$ and 2° from NGC 1399, respectively. For comparison, using their limiting magnitude of $R=22$ mag, we find a surface density of $0.3 \pm 0.1/\text{arcmin}^2$ at a radial distance of $16'$. Extrapolating our derived radial profile we would expect a surface density of $\approx 0.14/\text{arcmin}^2$ at $40'$ and of $\approx 0.02/\text{arcmin}^2$ at 2° . In particular at the larger radius we would expect a smaller number of GCs. This could be an indication that a population of "intergalactic clusters" exists, as proposed by Bassino et al. ((2002)).

9.3. Comparison of the NGC 1399 Light Profile with that of a "Normal" Elliptical

The luminosity profiles of many "normal" ellipticals follow a $r^{1/4}$ -de Vaucouleurs law. Here we have the opportunity to differentially compare NGC 1399 with such a "normal" galaxy, NGC 1404. This difference is illustrated in Fig. 20, where the profiles of NGC 1399 and of NGC 1404 are compared. We derived the luminosity profile of NGC 1404 in C and T1 in the same way as for NGC 1399. Care has been taken to take account of the extended halo of NGC 1399, which envelopes NGC 1404 fully in projection. We subtracted its contribution, i.e. the final luminosity profile, from each pixel. For the sky background the same value as for NGC 1399 has been used.

It can be seen that the light profile of NGC 1404, in contrast to NGC 1399, does not exhibit a uniform power law, but has an exponent of about -2 for radii smaller than $1.8'$ and -2.9 for larger radii, i.e. almost -4 in deprojection.

The deviation from a $r^{1/4}$ -de Vaucouleurs law is not unusual for galaxies brighter than $M_V = -21$. The light profile shapes of brighter galaxies become progressively more concave when plotted against $r^{1/4}$ (Kormendy & Djorgovski (1989)). These authors define a cD galaxy by a light profile, which exhibits an inflection point independent from the way it is plotted. In this sense, NGC 1399 would not be a cD galaxy.

Whatever the exact definition of a cD galaxy may be, it is useful for further insight to think about the physical reason of a de Vaucouleurs profile. Many "normal" elliptical galaxies can be well described by a Jaffe (1987) profile, which in projection resembles the de Vaucouleurs law, and which in space in the outer regions is characterized by a transition from a r^{-3} to a r^{-4} power law. Jaffe ((1987)) and White ((1987)) have shown that a r^{-4} power law emerges if the energy distribution function has a sharp break at the escape energy, given a nearly Keplerian potential.

NGC 1399 has a massive dark halo resembling the potential of an isothermal sphere out to a distance of at least 40 kpc, shown by the dynamics of the globular clusters (Paper II). The

temperature of the X-ray gas outside this radius remains isothermal (Jones et al. (1997)). Therefore, even if the exact shape of the potential is not known, we can at least conclude that the Keplerian regime is not reached out to the very faint surface brightnesses where our photometry becomes unreliable. Thus it is very tempting to relate the persistence of the r^{-3} profile to the dark halo of NGC 1399.

We therefore understand the "halo" of NGC 1399, which morphologically appears as a deviation from a de Vaucouleurs profile, not as an additional component but as the natural continuation of the galaxy profile in the isothermal potential of the dark matter halo. Thus the term "cD halo" might be misleading since it implies an additional stellar component.

Finally, we do not detect a color gradient for NGC 1404. This shows that the population composition of NGC 1404 is radially more homogeneous than that of NGC 1399. Additionally, this also demonstrates that the observed color gradient in NGC 1399 is not an artefact of an incorrect background subtraction.

9.4. Disentangling the Stellar Populations

Superior to the approach to relate the two observed red and blue cluster subpopulations to the integral galaxy light would be the comparison between clusters and the respective field populations that formed during the same star formation event. This is not possible in a direct way. However, we can follow a more indirect approach in which we model the galaxy C and R light profile using some simplifying assumptions. We assume the field population to be a superposition of only two populations, one corresponding to the blue clusters and one to the red clusters. These two field populations shall have the mean color of their corresponding cluster populations. The relation between the number of clusters and the luminosity of their corresponding field population will be called *intrinsic specific frequency* (ISF) and is measured with respect to the T1 filter.

It is not possible to fit both, the color and the luminosity profile, if both cluster populations would have the same constant ISF because of their different surface density profiles. In addition, to reproduce the color gradient requires to allow for a change of the properties of the red populations by either a radial color or radial local specific frequency dependence. We limit ourselves to consider a changing ISF for the red population, which might be the strongest assumption we make. Otherwise the problem would not be well constrained and many solutions could be found. We used the linear approximation $ISF \propto r$. A shallower variation, e.g. $ISF \propto \log(r)$ results in a too shallow color gradient. With a much steeper dependence, e.g. $ISF \propto r^2$ the model luminosity profile shows a considerable dip at the point where the light of the blue population begins to dominate the total light, which is also incompatible with the observations. A model that fits the data reasonably well is depicted in Fig. 21. A characteristic of any satisfactory model is that the ISF of the blue cluster population is much higher than that of the red one at smaller radii.

It is also possible to use the color and luminosity profile together with the density profiles of red

and blue clusters to derive the ISF for both clusters samples directly. However, the disadvantage of this approach is that it is much stronger influenced by noise. Nevertheless, it may serve as a consistency test and we include the results of this calculation in Fig. 21. This illustrates that the two methods agree well considering the uncertainties.

9.5. From Light Distribution to Mass Distribution

We note that the color gradient in NGC 1399 indicates a radial change in the stellar M/L profile. If the outer regions are more metal-poor the M/L value decreases towards larger radii. If one wants to use the luminosity profile to infer the mass profile, one has to account for this effect. For an estimation, we assume two populations with the same age of 12 Gyr of different mean metallicities: a metallicity of -0.4 dex (representing the inner part in accordance with the galaxy's color) and -1.4 dex (representing the outermost parts). Worthey's interpolation engine then gives for the respective M/L-values in R (Miller-Scalo IMF): 1.45 (-0.4 dex) and 1.23 (-1.4 dex). This means that the associated mass profile becomes somewhat steeper than what would be derived from the luminosity profile using a constant M/L. Thus an increase of the power law exponent from -1.83 to ≈ -2.2 is expected.

10. Summary and conclusions

We investigated the GCS of NGC 1399 in the bands Washington C and Kron R with the CTIO 4-m MOSAIC camera. The imaged area is $36' \times 36'$, thus being among the largest concerning GCS investigations.

The main findings of this study are:

- The relatively modest specific frequency of 5.1 ± 1.2 of the GCS of NGC 1399, already noted by Ostrov et al. ((1998)) is confirmed. The local specific frequency increases with radius and is higher for the blue than for the red clusters.
- The color distribution shows a very pronounced bimodal appearance. However, we argue that the blue peak might artificially be caused by the non-linear color metallicity relation in conjunction with the color scatter at a given metallicity.
- The surface density profile is shallower for the blue clusters than for the red clusters within 8 arcmin. Outside a radius of $8'$, both surface density profiles are not distinguishable.
- The galaxy light shows a colour gradient resembling the change of the surface density profiles of blue and red clusters. The galaxy light can be modeled with the simple assumption of only two populations, each traced by a cluster population of the same mean color. A model

consistent with the data has a constant ISF for the blue clusters and a radially increasing ISF for the red clusters.

- The brightest clusters do not show the pronounced bimodal color distribution of the fainter ones and have an at least as concentrated radial distribution as the red GCs.

NGC 1399 was one of the "classic" high specific frequency galaxies. It would be very interesting to perform new studies of the similar cases M87 and NGC 3311 in order to see whether their high specific frequency still withstand closer scrutiny. If not, central galaxies in galaxy clusters are perhaps not the places of extraordinarily high efficiency of globular cluster formation, for which they have been taken.

The GC color distribution, in particular bimodality alone is not very restrictive for galaxy formation scenarios. Various models have been published that explain the observed bimodality/metallicity distribution, e.g. Ashman & Zepf ((1992)) Forbes et al. ((1997)), Côté et al. ((2001)), Beasley et al. ((2002)). It is believed that bimodal color distributions can be used as an argument against monolithic collapse scenarios, for example Rhode & Zepf ((2001)). However, doubts remain: Samland et al. ((1997)) showed that also a monolithic collapse scenario result in populations that have different metallicity distributions.

Since the color distribution alone is not suitable to constrain formation scenarios it is necessary to use further information.

The close relation of the color gradient of NGC 1399 with the mean color of the GCS might be seen in favor of a strongly dissipative period during which the globular clusters and the stellar body of the galaxy were formed together. However, a counterargument is the radially increasing local specific frequency of the red clusters. During a dissipative collapse one would expect the star formation rate to be highest where the density is highest, i.e in the central regions. Accordingly, also the efficiency of globular cluster formation should decrease radially outwards, if the star formation rate is a determining parameter (Larsen & Richtler (2000)).

Additionally, one has to take into account the kinematic and dynamical properties of the GCS. These are (Paper II): blue and red clusters show different velocity dispersions in accordance with their different surface density profiles. The orbit distribution is nearly isotropic. Only the outer blue clusters (if any) show signatures of rotation. The overall mass distribution resembles an isothermal sphere.

Thus some sort of relaxation mechanism must have been active in the early times of NGC 1399, which is difficult to find in a purely dissipative collapse, but naturally provided by a phase of violent relaxation during a merger. The merger components (probably more than only 2) could have been gas-rich, unevolved metal-poor galaxies where cluster formation was efficient during the starburst preceding the merger itself. In addition to the (presumably mainly metal poor) cluster populations of the merger components, the bulk of clusters, both metal-rich and metal-poor, could have been formed during this period. These clusters have after the merging took place roughly the

same spatial distribution. However, after the merger remnant has reached its equilibrium, cluster formation continued in the inner regions, albeit with a decreased efficiency, forming the metal rich part of the inner red cluster population.

Based on this idea we can estimate the number of additional red globular clusters. For this we assume that we have one population of metal rich clusters that have the same density profile as the blue ones (albeit with a different normalization taken from the red clusters at radii larger than 8'). Then we require ≈ 700 additional red clusters to explain the difference between the two profiles.

Acknowledgments

We acknowledge the help of M.Shara, D.Zurek and E.Grebel, who obtained some MOSAIC images that were used in this investigation. BD gratefully acknowledges financial support of the Alexander-von-Humboldt Foundation via a Feodor Lynen Stipendium. DG and WPG gratefully acknowledge support from the Chilean Center for Astrophysics FONDAP No. 15010003. We thank an anonymous referee for helpful comments.

References

Arimoto, N., Yoshii, Y., 1987, A&A 173, 23

Ashman, K.M., Zepf, S.E., 1992, ApJ 384, 50

Ashman, K.M., Zepf, S.E., 1993, MNRAS 264, 611

Ashman, K.M., Conti, A., Zepf, S.E., 1995, AJ 110, 1164

Ashman, K.M., Zepf, S.E., 1998, "Globular Cluster Systems", Cambridge Astrophysics Series, Cambridge University Press

Bassino L.P., Cellone S.A., Forte J.C., Dirsch B., 2002, A&A submitted

Beasley, M.A., Baugh, C.M., Ducan, A.F. et al., 2002, MNRAS 333, 383

Bekki, K., Forbes, D.A., Beasley, M.A., Couch, W.J., 2002, astro-ph/0206008, MNRAS in press

Bertin, E., Arnouts, S., 1996, A&AS 117, 393

Bridges, T.J., Hanes, D.A., Harris, W.E., 1991, AJ 101, 469

Brodie J.P., Larsen S.S., Kissler-Patig M., 2000, ApJ 543, L19

Buote, D.A., 2000, MNRAS 311, 176

Caon, N., Capaccioli, M., D'Onofrio, M., 1994, A&AS 106, 199

Côté, P., McLaughlin, D.E., Hanes, D.A., et al., 2001 ApJ 559, 828

Côté, P., West, M.J., Marzke, R.O., 2002, ApJ 567, 853

Dawe, J.A., Dickens, R.J., 1976, Nature 263, 395

Elmegreen, B.G., 1999, Ap&SS 269, 469

Faber, S.M., Wegner, G., Burstein, D. et al., 1989 ApJS 69, 763

Forbes, D.A., Brodie, J.P., Grillmair, C.J., 1997, AJ 113, 1652

Forbes, D.A., Grillmair, C.J., Williger, G.M. et al., 1998, MNRAS 293, 325

Forbes, D.A., Forte, J.C., 2001, MNRAS 322, 257

Forbes, D.A., Beasley, M.A., Brodie, J.P., Kissler-Patig M., 2001, ApJ 563, L143

Forte, J.C., Geisler, D., Ostrov, P.G. et al., 2001, AJ 121, 1992

Gebhardt, K., Kissler-Patig, M., 1999, AJ 118, 1526

Geisler, D., 1996, AJ 111, 480

Geisler, D., Lee, M.G., Kim, E., 1996, AJ 111, 1529

Grillmair, C.J., Freeman, K.C., Bicknell, G.V., et al., 1994, ApJ 422, L9

Grillmair, C.J., Forbes, D.A., Brodie, J.P., Elson, R.A.W., 1999, AJ 117, 167

Hanes, D.A., Harris, W.E., 1986, ApJ 309, 564

Harris, H.C., Canterna, R., 1977, AJ 82, 798

Harris, W.E., van den Bergh, S., 1981, ApJ 309, 654

Harris, W.E., Hanes, D.A., 1987, AJ 93, 1368

Harris, W.E., Allwright, J.W.B., Pritchett, C.J., van den Bergh, S., 1991, ApJS 76, 115

Harris, W.E., Hanes, D.A., 1987, CDS VizieR On-line Data Catalog: VII/195

Harris, W.E., Kavelaars, J.J., Hanes, D.A. et al., 2000, ApJ 533, 137

Harris, W.E., 2001, in "Star Clusters", Saas-Fee Advanced Course 28, Lecture Notes 1998, eds. L. Labhardt and B. Binggeli, Springer-Verlag, Berlin, p.223

Harris W.E., Harris G.L.H., 2002, AJ 123, 3108

Hilker, M., Infante, L., Richtler, T., 1999, A&AS 138, 55

Idiart, T.P., Michard, R., de Freitas Pacheco, J.A., 2002, A&A 383, 30

Jaffe, W., 1987, in "Structure and Dynamics of Elliptical Galaxies", IAU Symp. 127, ed. T. de Zeeuw, D. Reidel, Dordrecht, p.511

Jones, C., Stern, C., Forman, W., 1997, ApJ 482, 143

Killeen, N.E.B., Bicknell, G.V., 1988, ApJ 325, 165

Kissler, M., Richtler, T., Held, E. et al., 1994, A&A 287, 463

Kissler-Patig, M., Kohle, S., Hilker, M. et al., 1997, A&A 319, 470

Kormendy, J., Djorgovski, S., 1989, ARAA 27, 235

Kundu, A., Whitmore, B.C., 2001a, AJ 121, 2950

Kundu, A., Whitmore, B.C., 2001b, AJ 122, 1251

Larsen, S.S., Richtler, R., 1999, A&A 345, 59

Larsen, S.S., Richtler, R., 2000, A&A 354, 836

Larsen, S.S., Brodie, J.P., Huchra, J.P. et al., 2001, AJ 121, 2974

Lauberts, A., Valentijn, E.A., 1989, "The surface photometry catalogue of the ESO-Uppsala galaxies", European Southern Observatory, Garching

Lauer, T.R., Ajhar, E.A., Byun, Y. et al., 1995, AJ 110, 2622

Liu, M.C., Graham, J.R., Charlot, S., 2002, ApJ 564, 216

McLaughlin, D.E., 1999, AJ 117, 2398

Mackie, G., Visvanathan, N., Carter, D., 1990, ApJS 73, 637

Merritt, D., Tremblay, B., 1994, AJ 111, 2243

Ostrov, P.G., Geisler, D., Forte, J.C., 1993, AJ 105, 1762

Ostrov, P.G., Forte, J.C., Geisler, D., 1998, AJ 116, 2854

Pagel B.E.J., 1997, Nucleosynthesis and Chemical Evolution of Galaxies, Cambridge University Press

Persson, S.E., Frogel, J.A., Aaronson, M., 1979, ApJS 39, 61

Poulain, P., 1988, A&AS 72, 215

Richtler, T., Drenkhahn, G., Gómez, M., Seggewiss, W., 2000, in "From Extrasolar Planets to Cosmology: The VLT Opening Symposium", eds. J. Bergeron and A. Renzini, Springer Verlag, Berlin, p. 259

Richtler, T., Dirsch, B., Geisler, D. et al., 2001, IAU Symp. 207, "Extragalactic Star Clusters", eds. Geisler D., Grebel E.K., Minniti D., p. 263

Richtler, T., Dirsch, B., Gebhardt, K. et al., 2002, (Paper II), submitted to AJ

Rhode, K.L., Zepf, S.E., 2001, AJ 121, 210

Samland, M., Hensler, G., Theis, Ch., 1997, ApJ 476, 544

Schlegel, D., Finkbeiner, D., Davis, M., 1998, ApJ 500, 525.

Schombert, J.M., 1986, ApJS 60, 603

Secker J., Geisler D., McLaughlin D.E., Harris W.E., 1995, AJ 109, 1019

Tonry, J.L., Dressler, A.D., Blakeslee, J.P. et al., 2001, AJ 546, 681

Valentijn, E.A., 1983, A&A 118, 123

van den Bergh, S., 2000, PASP 112, 932

Wagner, S., Richtler, T., Hopp, U., 1991, A&A 241, 399

West M.J., Côté P. Jones C. et al., 1995, AJ 453, L77

White III R.E., 1987, MNRAS 227, 185

White, S.D.M., 1987, in "Structure and Dynamics of Elliptical Galaxies", IAU Symp. 127, ed. T. de Zeeuw, D. Reidel, Dordrecht, p.263

Whitmore, B.C., Schweizer, F., 1995, AJ 109, 960

Worley, G., 1994, ApJS 95, 107

Zepf, S.E., Ashman, K.M., 1993, MNRAS 264, 611

Zepf, S.E., Ashman, K.M., Geisler D., 1995, ApJ 443, 570

Table 1. Observational data used in this investigation.

Telescope	Date	right ascension	declination	Filter	Exposure time	Seeing
MOSAIC	7.12.1999	3°38'12".0	-35 ^h 32 ^m 25 ^s	R	420 sec	1.1"
MOSAIC	7.12.1999	3°38'12".0	-35 ^h 32 ^m 25 ^s	R	420 sec	1.0"
MOSAIC	7.12.1999	3°38'12".0	-35 ^h 32 ^m 25 ^s	R	420 sec	0.9"
MOSAIC	11.12.1999	3°38'12".0	-35 ^h 32 ^m 25 ^s	R	420 sec	1.2"
MOSAIC	11.12.1999	3°38'12".0	-35 ^h 32 ^m 25 ^s	R	420 sec	1.2"
MOSAIC	11.12.1999	3°38'12".0	-35 ^h 32 ^m 25 ^s	R	420 sec	1.3"
MOSAIC	12.12.1999	3°38'12".0	-35 ^h 32 ^m 25 ^s	R	420 sec	1.2"
MOSAIC	15.12.1999	3°38'12".0	-35 ^h 32 ^m 26 ^s	C	1500 sec	1.1"
MOSAIC	15.12.1999	3°38'13".0	-35 ^h 32 ^m 15 ^s	C	1500 sec	1.1"
MOSAIC	15.12.1999	3°38'13".0	-35 ^h 32 ^m 32 ^s	C	1500 sec	1.0"
VLT	1.12.2000	3°38'45"	-35 ^h 23 ^m 30 ^s	V	300 sec	0.55"
VLT	1.12.2000	3°38'45"	-35 ^h 23 ^m 30 ^s	I	300 sec	0.55"
VLT	2.12.2000	3°38'08"	-35 ^h 31 ^m 00 ^s	V	300 sec	0.64"
VLT	2.12.2000	3°38'08"	-35 ^h 31 ^m 00 ^s	I	300 sec	0.6"
VLT	3.12.2000	3°37'30"	-35 ^h 31 ^m 30 ^s	V	300 sec	0.56"
VLT	3.12.2000	3°37'30"	-35 ^h 31 ^m 30 ^s	I	300 sec	0.5"
MOSAIC	31.12.1999	3°48'00".0	-35 ^h 35 ^m 00 ^s	R	120 sec	1.0"
MOSAIC	31.12.1999	3°48'00".0	-35 ^h 35 ^m 00 ^s	R	600 sec	1.0"
MOSAIC	31.12.1999	3°48'00".0	-35 ^h 35 ^m 00 ^s	C	1800 sec	1.0"

Table 2. Color distribution of clusters for the whole sample (N_{all}), within $1.8' < r < 4.5'$ (N_1), within $4.5' < r < 13.5'$ (N_2) and $r > 13.5'$ (N_3).

C-R	N_{all}	N_1	N_2	N_3	N_{BG}
0.8	14 ± 13	2 ± 2	10 ± 7	4 ± 8	80 ± 9
0.9	60 ± 18	6 ± 3	31 ± 9	26 ± 11	129 ± 11
1	53 ± 18	10 ± 4	41 ± 11	3 ± 11	135 ± 12
1.1	169 ± 20	31 ± 6	96 ± 13	42 ± 12	119 ± 11
1.2	384 ± 24	59 ± 8	203 ± 16	119 ± 15	108 ± 10
1.3	458 ± 25	73 ± 9	253 ± 17	123 ± 14	87 ± 9
1.4	360 ± 22	72 ± 9	187 ± 15	88 ± 12	53 ± 7
1.5	223 ± 17	50 ± 7	109 ± 11	50 ± 9	42 ± 6
1.6	236 ± 17	55 ± 7	111 ± 11	55 ± 9	23 ± 5
1.7	186 ± 15	59 ± 8	83 ± 10	37 ± 7	19 ± 4
1.8	219 ± 16	72 ± 8	95 ± 10	41 ± 7	15 ± 4
1.9	156 ± 13	50 ± 7	68 ± 9	24 ± 6	10 ± 3
2	108 ± 12	37 ± 6	45 ± 7	15 ± 5	13 ± 4
2.1	39 ± 8	9 ± 3	18 ± 5	4 ± 3	9 ± 3
2.2	14 ± 6	7 ± 2	1 ± 3	4 ± 4	12 ± 3
2.3	5 ± 4	1 ± 1	3 ± 2	1 ± 1	5 ± 2

Table 3. Observed radial number density of red ($n(\text{red})$) and blue ($n(\text{blue})$) clusters.

$\log(r[\text{arcmin}])$	$\log(n(\text{red})[\text{arcmin}^{-2}])$	$\log(n(\text{blue})[\text{arcmin}^{-2}])$
0.24	1.13 ± 0.06	0.61 ± 0.10
0.31	1.04 ± 0.05	0.54 ± 0.09
0.38	0.82 ± 0.06	0.56 ± 0.08
0.45	0.89 ± 0.05	0.39 ± 0.09
0.52	0.69 ± 0.06	0.26 ± 0.10
0.59	0.58 ± 0.06	0.40 ± 0.07
0.66	0.46 ± 0.05	0.24 ± 0.07
0.73	0.33 ± 0.05	0.28 ± 0.06
0.80	0.32 ± 0.05	0.14 ± 0.06
0.87	0.20 ± 0.05	0.10 ± 0.05
0.94	-0.13 ± 0.06	-0.08 ± 0.06
1.01	-0.30 ± 0.06	-0.23 ± 0.06
1.08	-0.26 ± 0.06	-0.19 ± 0.05
1.15	-0.42 ± 0.06	-0.24 ± 0.05
1.22	-0.43 ± 0.06	-0.57 ± 0.08
1.29	-0.45 ± 0.06	-0.72 ± 0.10
1.36	-0.75 ± 0.10	-0.88 ± 0.13

Table 4. The final luminosity profile of NGC 1399 plotted in Fig.14. The second column gives the surface brightness at the radius given in the first column. The third column gives the ellipticity and the fourth column the integrated magnitudes at selected radii. The last column shows the C-T1-color.

$\log(r[\text{arcmin}])$	$T1 [\text{arcsec}^{-2}]$	ellipticity	$T1 [\text{mag}]$	C-T1
-3.436	15.39	0
-2.436	15.48	0.13
-2.115	15.59	0.13
-1.757	15.78	0.062
-1.405	16.19	0.085
-1.052	16.99	0.12
-1.015	11.38	
-0.7095	18.14	0.13
-0.4893	19.05	0.11
-0.2939	19.84	0.11
-0.1183	20.56	0.09
0.0	9.43	...
0.04123	21.27	0.07	...	1.71
0.3299	22.43	0.09	...	1.64
0.5136	23.18	0.11	...	1.55
0.6422	23.69	0.20	...	1.41
0.7413	24.14	0.20	...	1.36
0.75	8.48	...
0.822	24.63	0.20	...	1.13
0.89	24.91	0.20	...	1.19
0.9488	25.22	0.20	...	1.17
1.001	25.31	0.20	...	1.29
1.047	25.69	0.20	...	1.03
1.05	8.20	...
1.089	26.03	0.20	...	1.05
1.123	26.24	0.20
1.191	26.21	0.20
1.292	26.75	0.20
1.292	8.08	...

Table 5. Local specific frequency for the whole sample (second column), the red subpopulation (third column), and the blue sample (last column). The errors include the error of the luminosity profile and Poisson counting statistics.

$\log(r[\text{arcmin}])$	$S_R(\text{all})$	$S_R(\text{red})$	$S_R(\text{blue})$
0.26	4.3 ± 0.4	2.6 ± 0.32	1.7 ± 0.3
0.43	5.8 ± 0.7	3.3 ± 0.5	2.5 ± 0.5
0.56	6.9 ± 1.0	3.7 ± 0.7	3.2 ± 0.7
0.65	7.0 ± 1.2	3.3 ± 0.8	3.7 ± 0.9
0.73	8.2 ± 1.5	3.7 ± 1.0	4.5 ± 1.1
0.80	9.1 ± 1.9	4.0 ± 1.3	5.1 ± 1.4
0.86	9.8 ± 2.3	4.7 ± 1.6	5.1 ± 1.6
0.91	9.3 ± 2.4	3.4 ± 1.5	6.0 ± 1.9
0.95	7.5 ± 2.4	3.3 ± 1.6	4.1 ± 1.8
1.00	8.1 ± 2.7	2.8 ± 1.6	5.3 ± 2.2
1.03	6.4 ± 2.7	3.3 ± 1.9	3.1 ± 1.9
1.07	10.8 ± 3.9	4.9 ± 2.7	5.9 ± 2.9
1.10	14.2 ± 5.0	4.9 ± 2.9	9.2 ± 4.0
1.13	12.6 ± 5.0	5.5 ± 3.3	7.1 ± 3.7
1.16	11.8 ± 5.4	5.3 ± 3.6	6.5 ± 4.0
1.20	18.3 ± 9.0	9.9 ± 6.6	8.4 ± 6.1

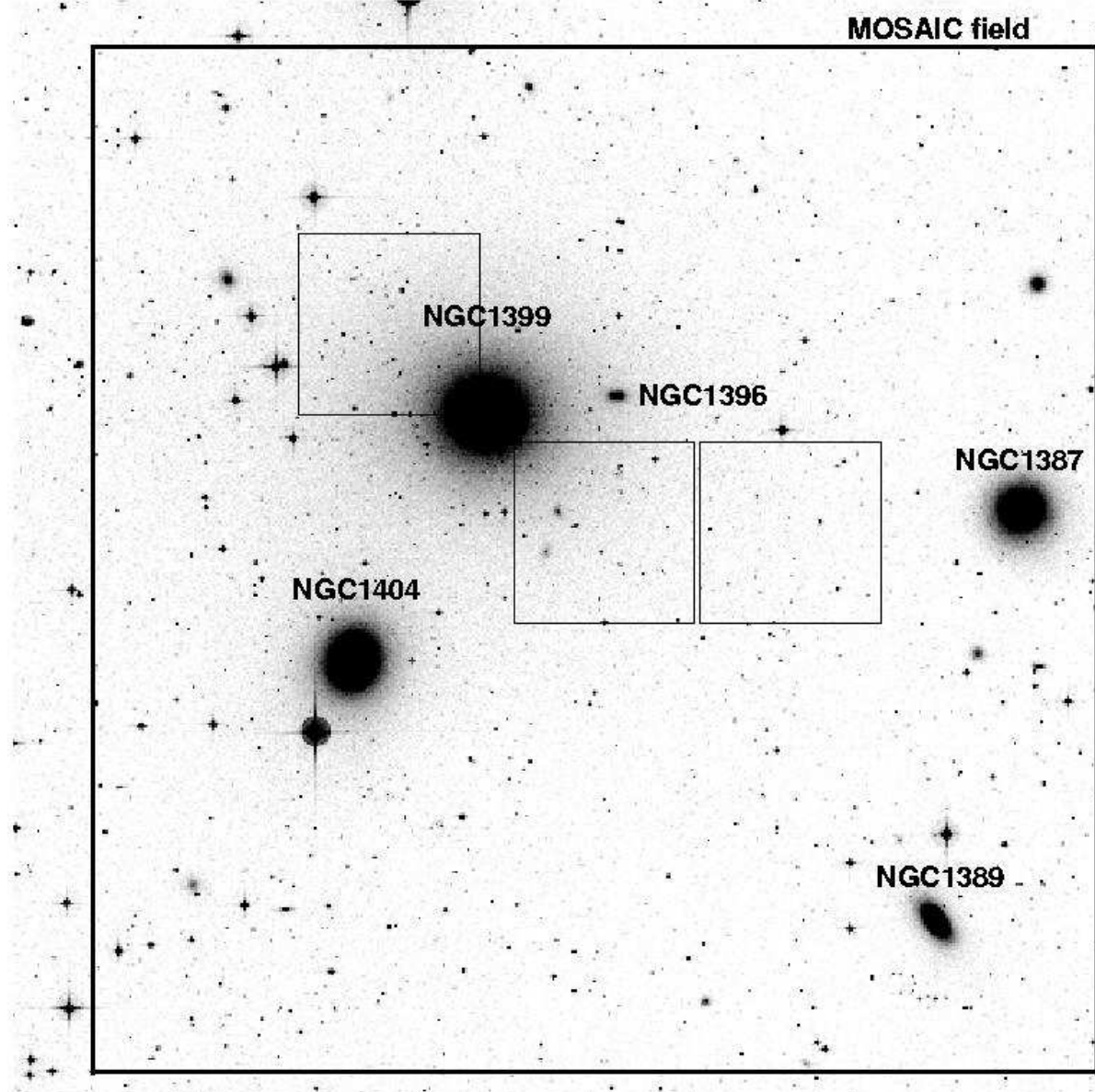


Fig. 1.— The MOSAIC field and the three smaller VLT fields are overlaid on a DSS image.

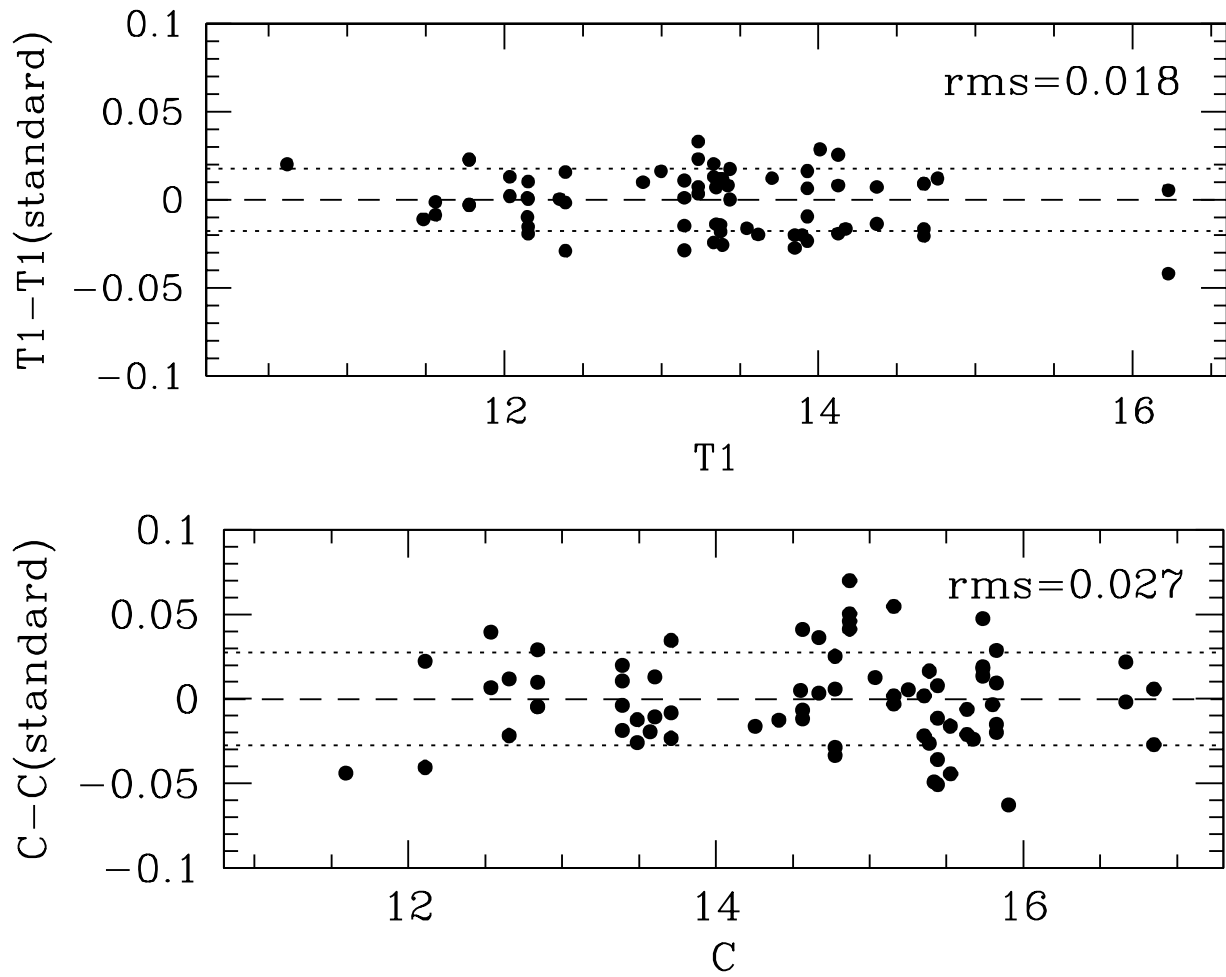


Fig. 2.— The residuals of the standard star magnitudes after the applied calibration are plotted.

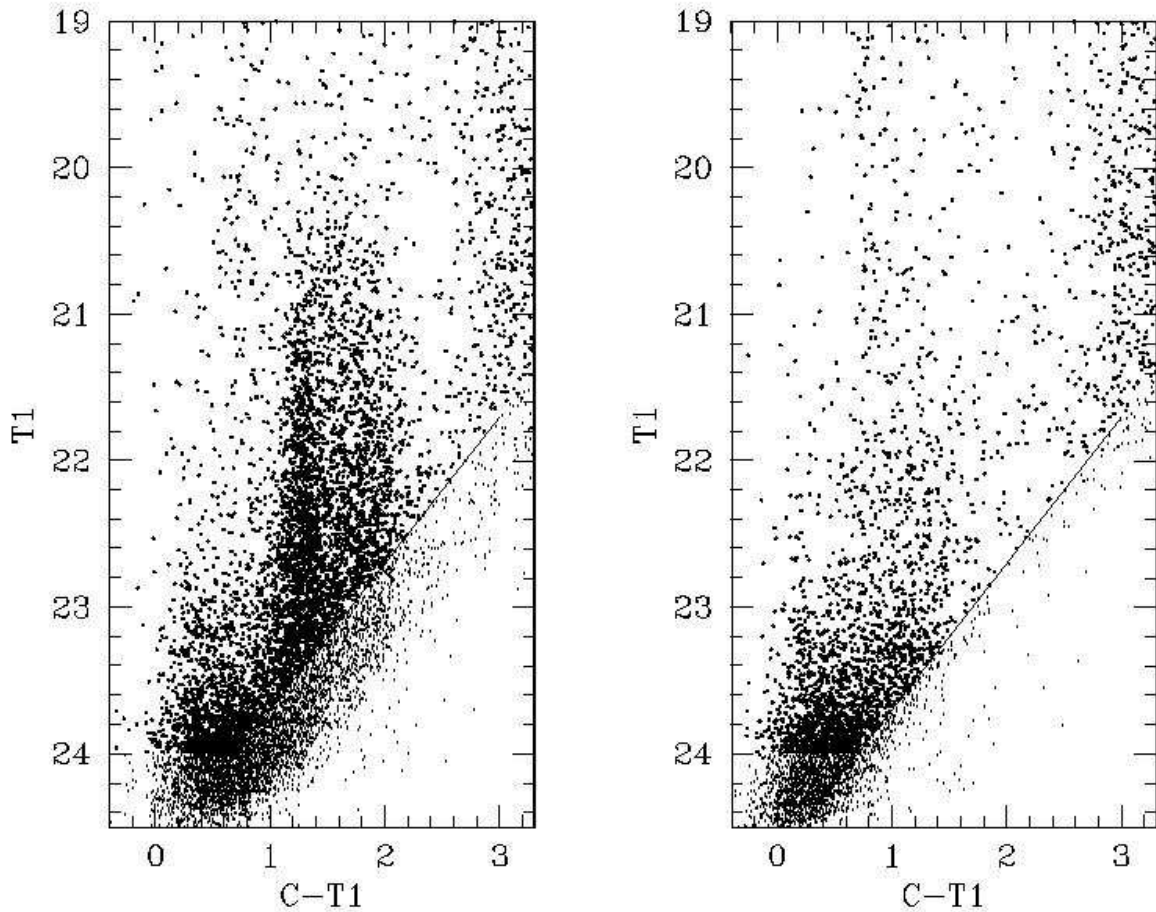


Fig. 3.— The CMD based on the MOSAIC data is shown in the left panel for the NGC 1399 field, and in the right panel for the background field. The line indicates the limiting magnitude which is used throughout the paper. Brighter stars are also plotted with slightly thicker dots than stars fainter than the limiting magnitude.

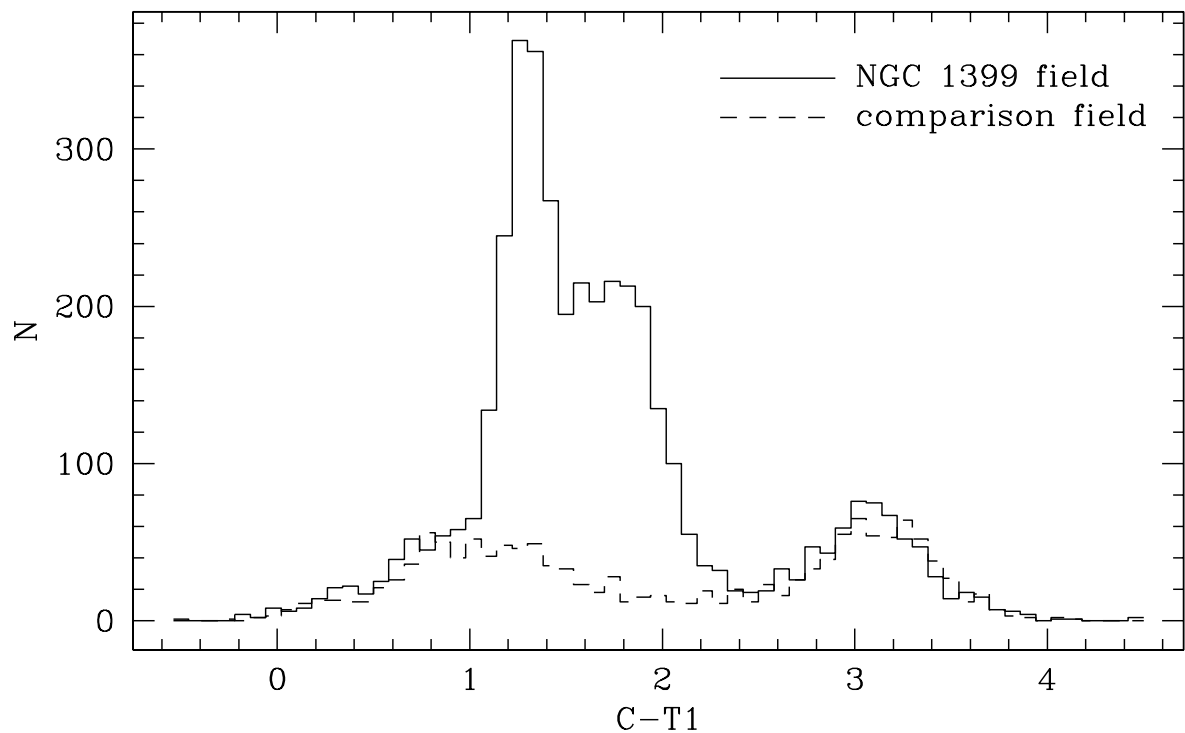


Fig. 4.— Comparison of the color histograms of all selected point sources of the NGC 1399 field (solid line) and the comparison field (dashed line).

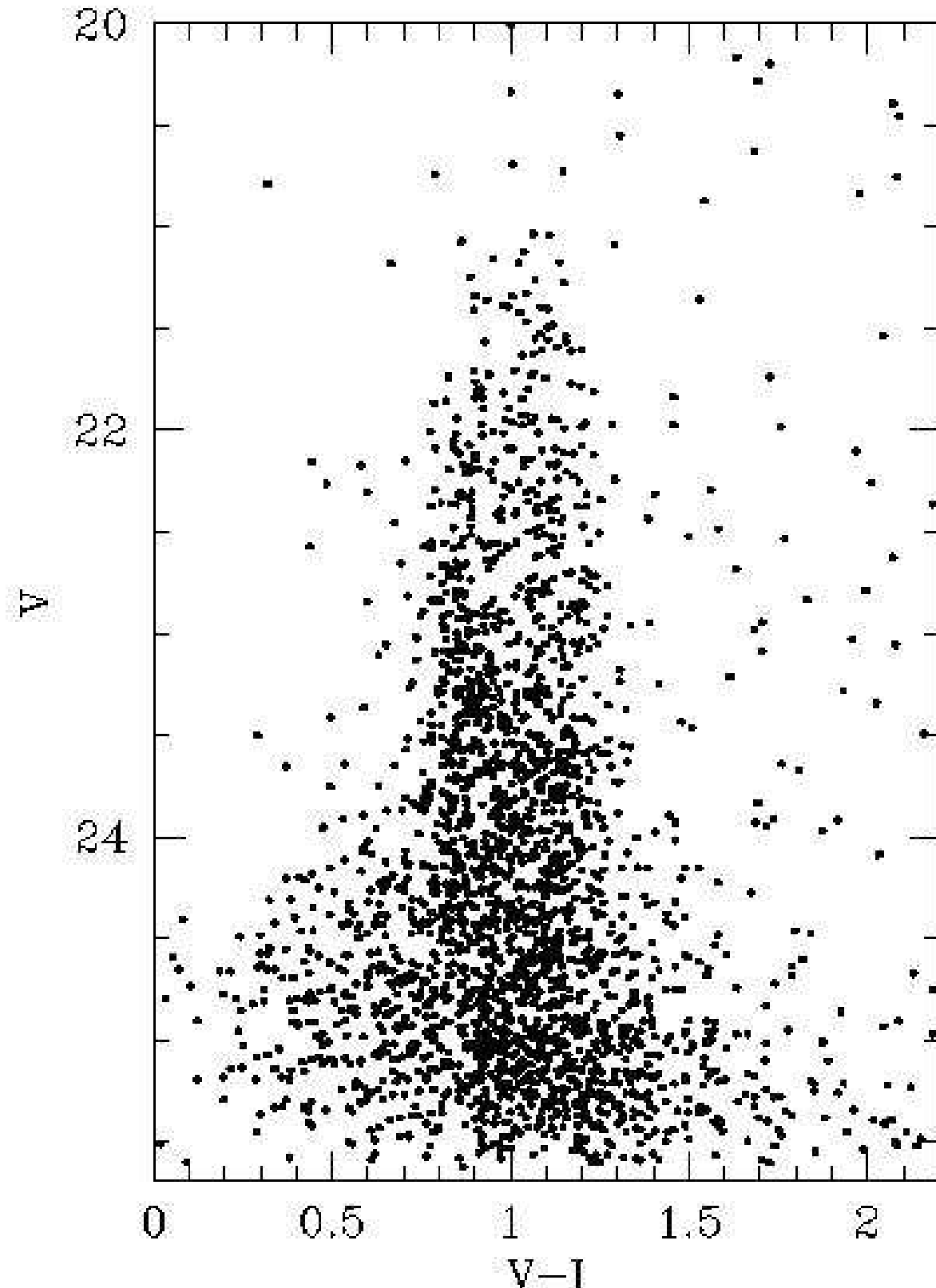


Fig. 5.— The CMD assembled from the three VLT fields. The bimodality of the color distribution is visible, although not as nicely as in the Washington colors (Fig.3). We shall use the VLT photometry mainly for deriving the globular cluster luminosity function.

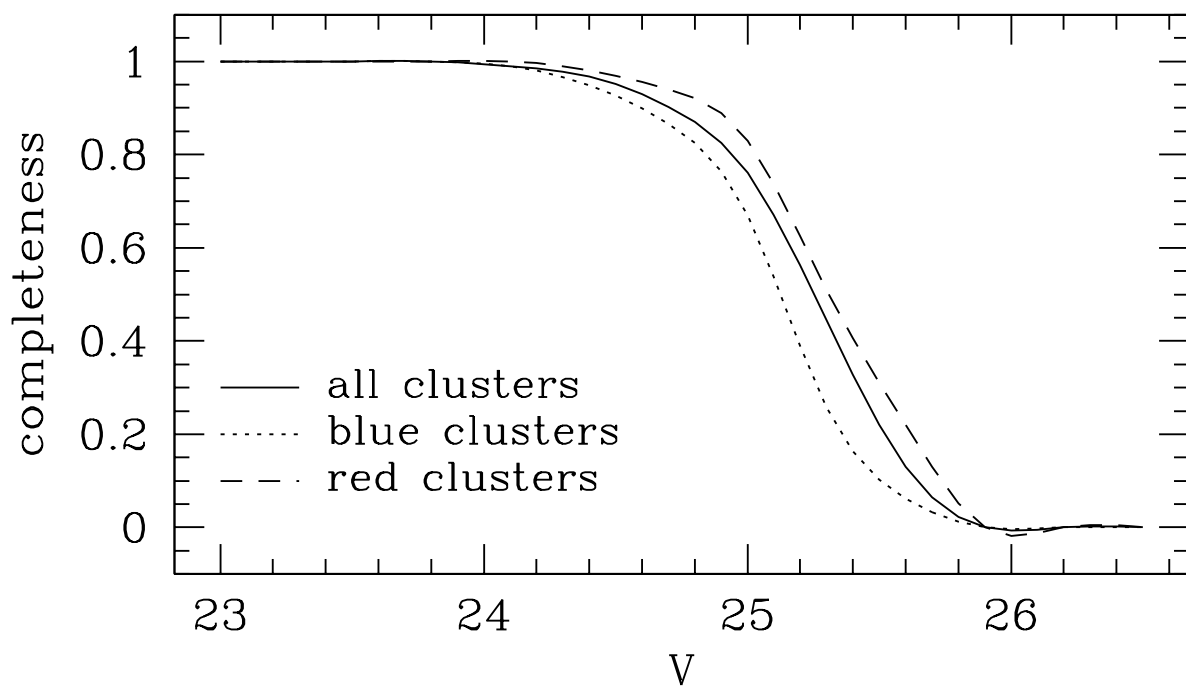


Fig. 6.— Completeness function for the VLT data (Field 1).

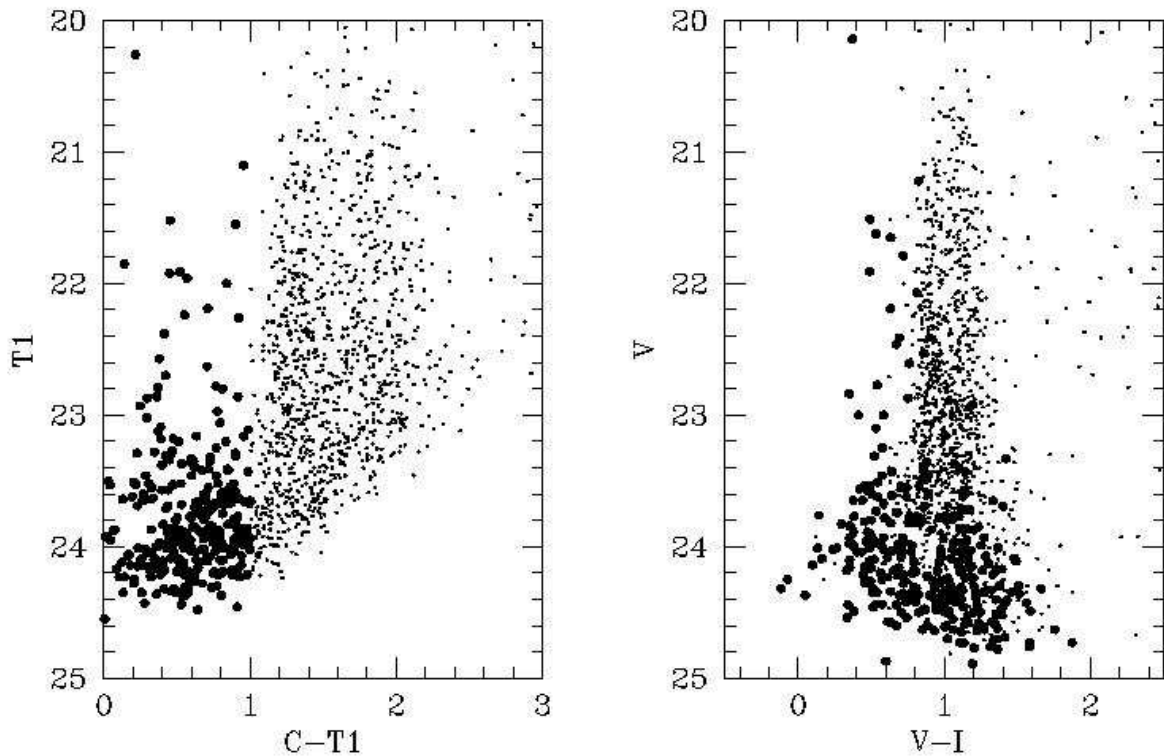


Fig. 7.— The CMDs of point sources that have been identified on both the VLT and the MOSAIC images. We marked objects bluer than $C-T1=1$ by filled circles. These are predominantly galaxies. Note how these objects contaminate the CMD in $V,V-I$.

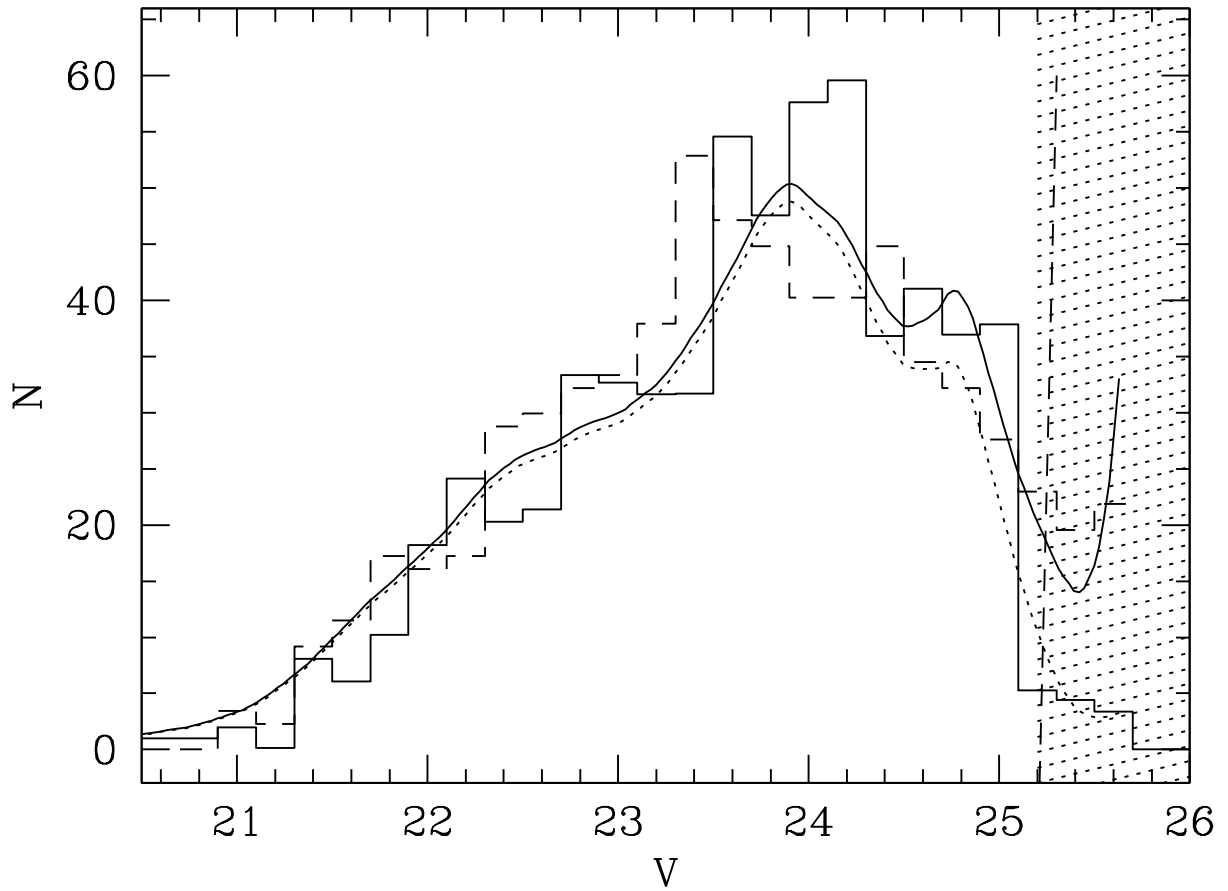


Fig. 8.— The luminosity function of the cluster candidates within a adial range of $4.3'$ in the FORS2 images is plotted as solid line. The shaded area designates the magnitude range beyond the 50% completeness. The dotted line shows the histogram before the completeness correction. The dashed histogram indicates the (arbitrarily scaled) HST GC luminosity function of Grillmair et al. ((1999)).

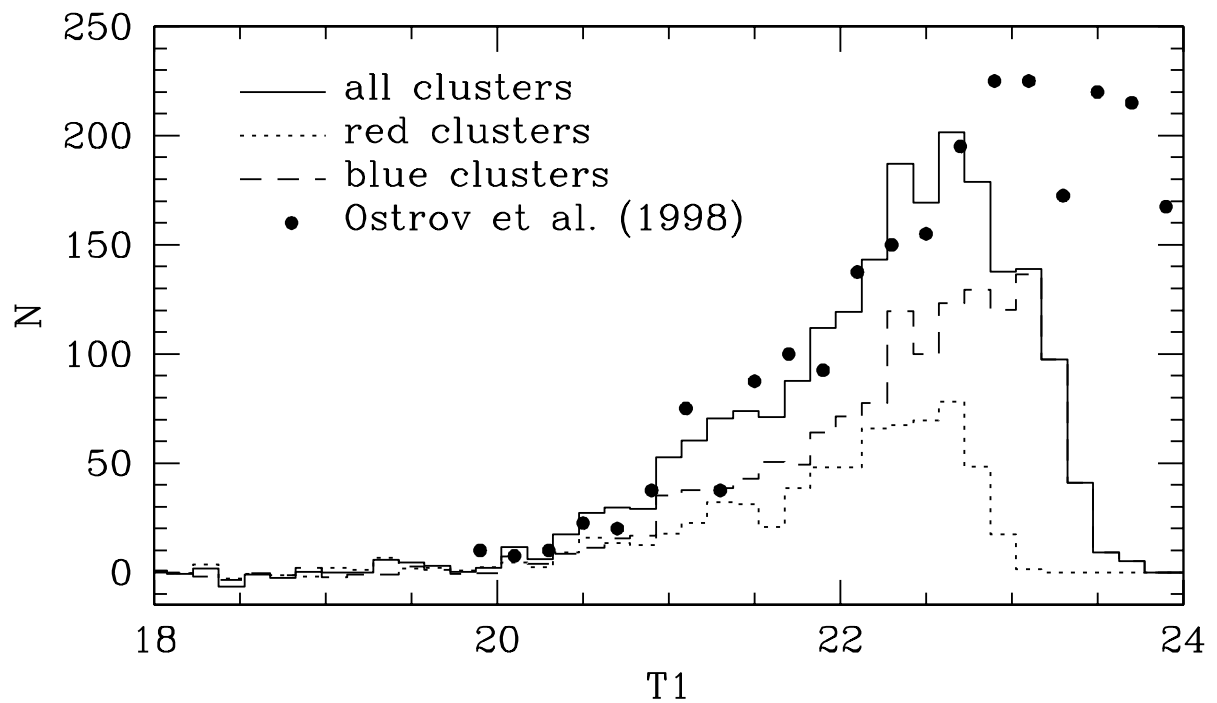


Fig. 9.— The luminosity function of the cluster candidates from the MOSAIC data is shown for the whole sample (solid line), and the blue and red subsamples (dotted and dashed line, respectively). The luminosity function given by Ostrov et al. ((1998)) is also shown (arbitrarily scaled).

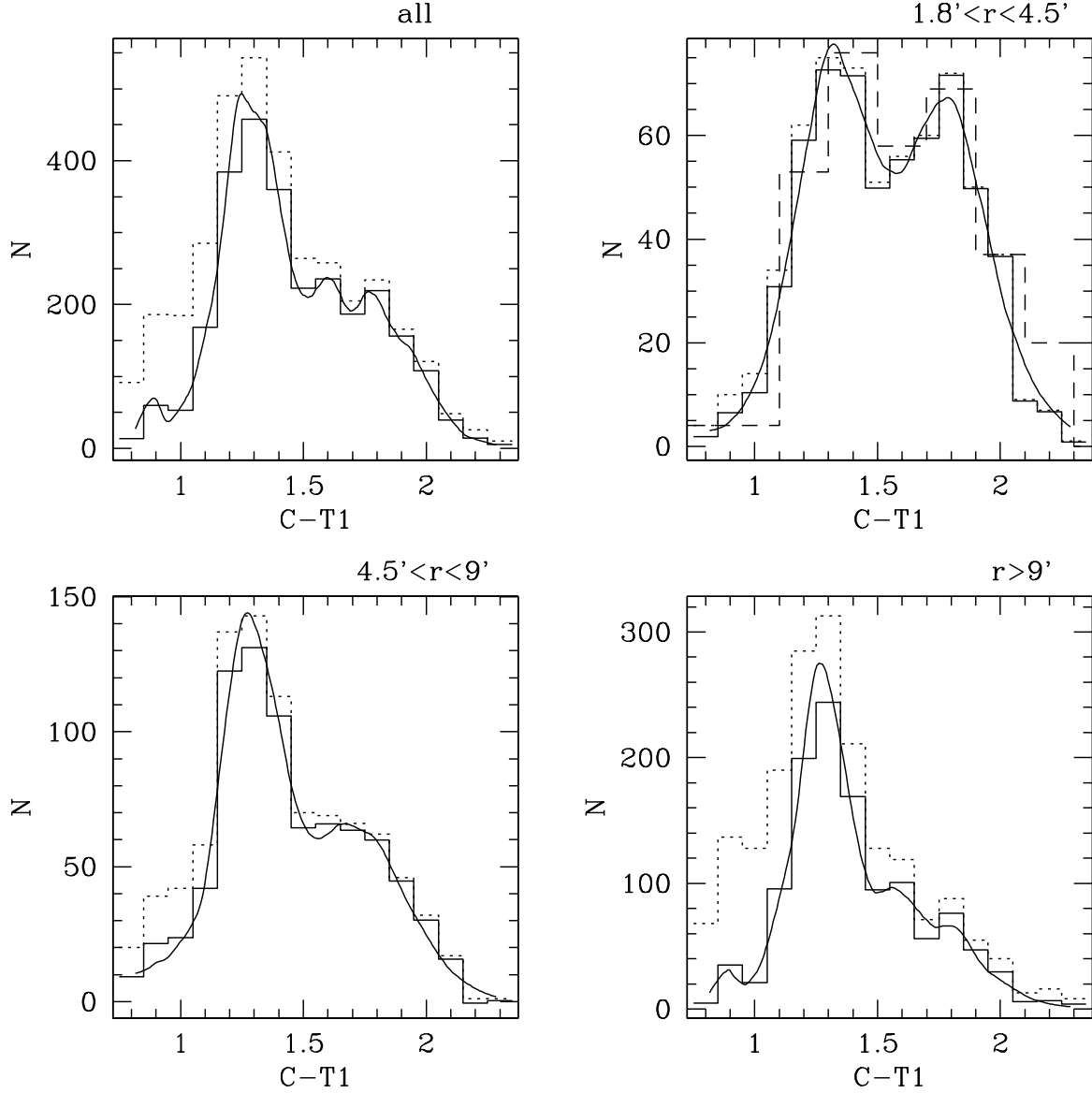


Fig. 10.— The color distribution of globular clusters is plotted for the entire sample and, for three samples within different radial intervals which are indicated at the upper right of each panel. The dotted histogram shows the distribution before the statistical background subtraction. The smooth line is the adaptive kernel filtered distribution (described in Sect.4). The dashed histogram in the upper right panel shows the color distribution by Ostrov et al. ((1998)) within the same area and demonstrates the good agreement of the photometry. The counts of Ostrov et al. have not been scaled. For an interpretation of these observed distributions see Sect. 5 of the text.

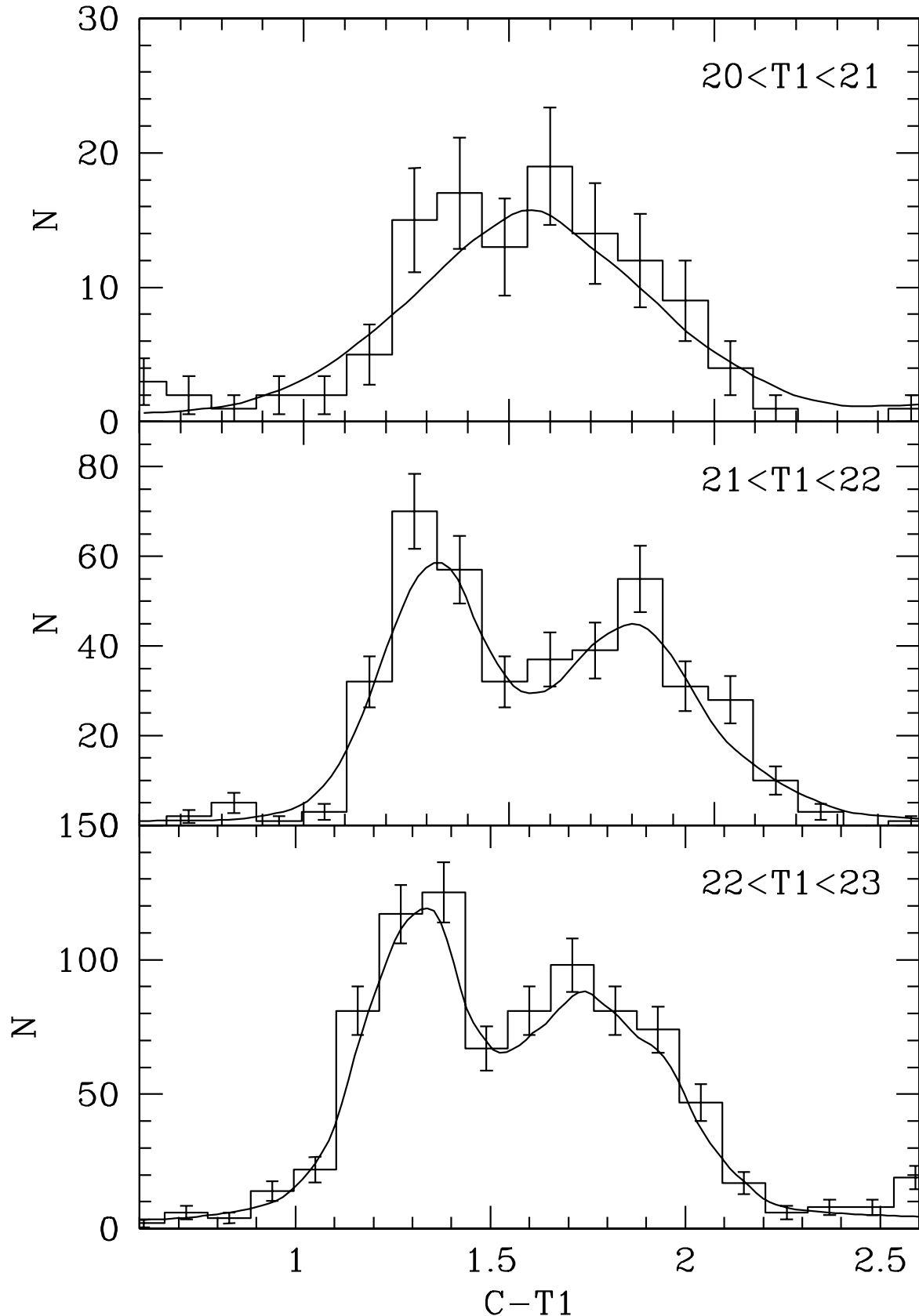


Fig. 11.— The color distribution of globular clusters is plotted for three different luminosity

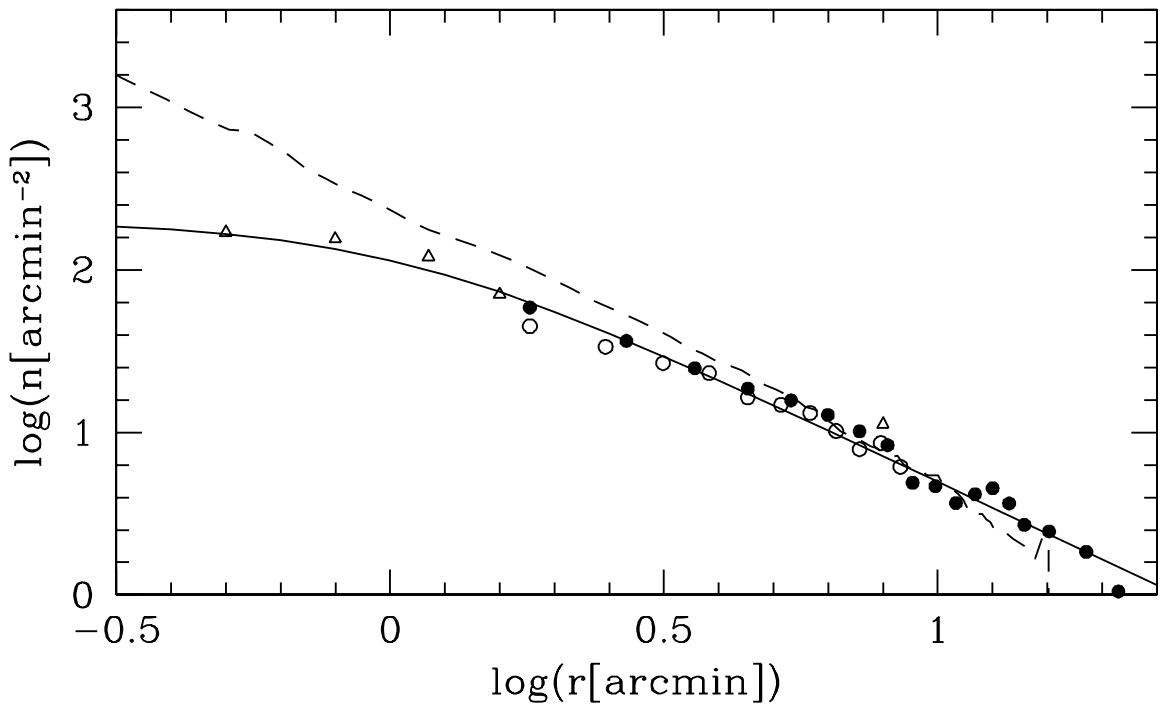


Fig. 12.— This plot shows the radial density distribution of all clusters (extrapolated to the entire luminosity function) derived from the MOSAIC data (open circles), the VLT data (filled circles) and from HST data (triangles, Forbes et al. (1998)). The solid line is the fit to the data. The dashed line shows the luminosity profile of NGC 1399, which is described in Sec.7.

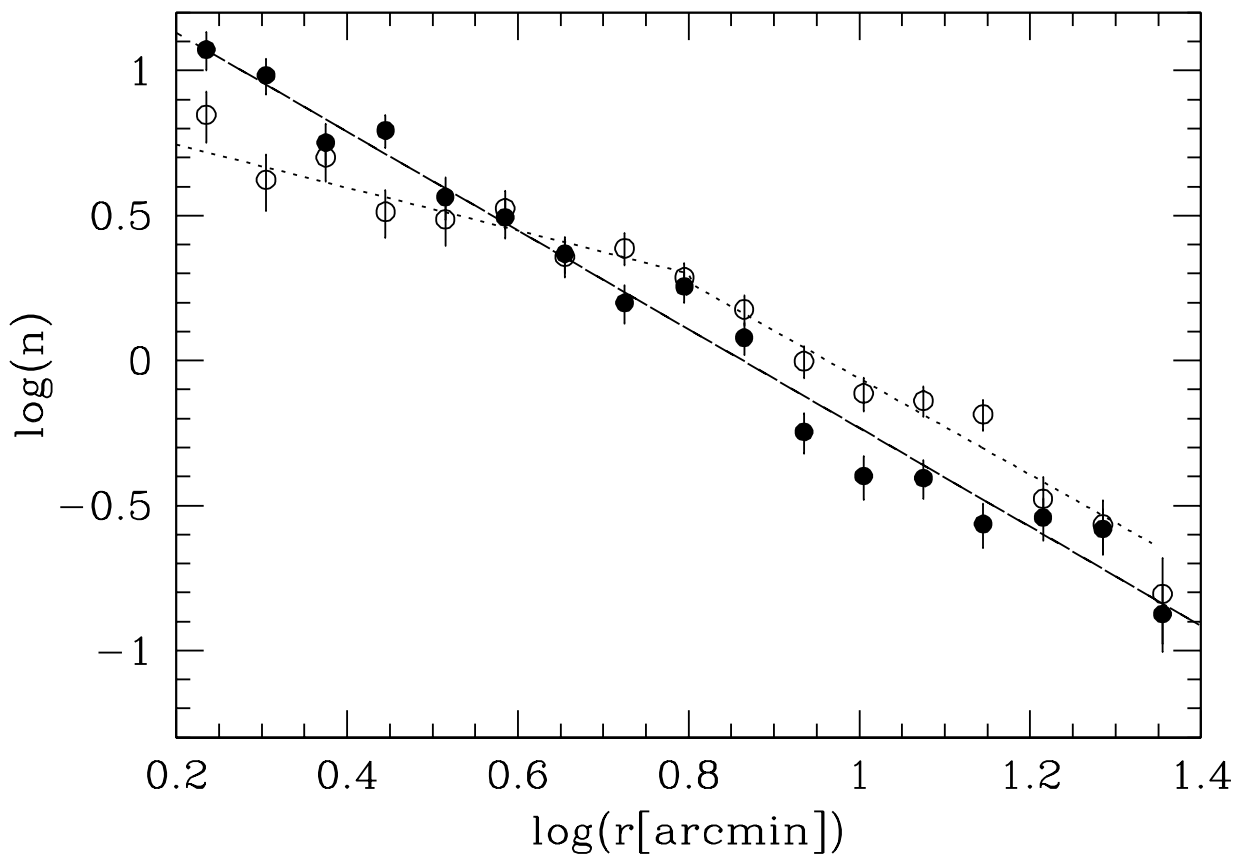


Fig. 13.— The radial density profiles of the observed number of red (filled circles) and blue (open circles) globular clusters detected on the MOSAIC image are plotted together with the fitted power-laws. The counts are tabulated in Tab.3.

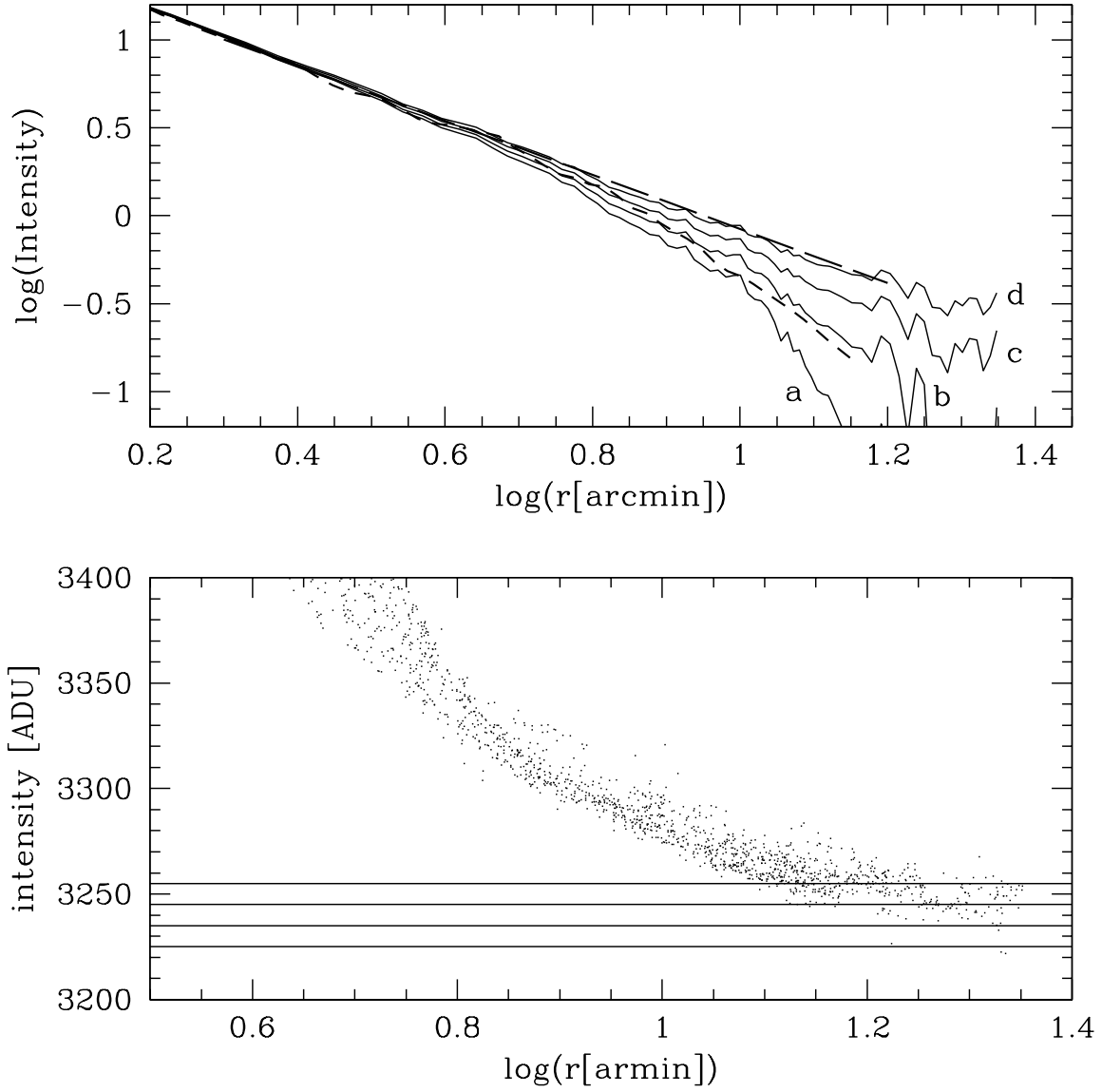


Fig. 14.— The luminosity profile from our R images (solid lines, for four different background values), the one published by Schombert et al. ((1986), short dashed line) and the one by Caon et al. ((1994), long dashed line). We shifted all profiles to the B surface magnitude given by Caon et al. within the radial range of $1'$ to $1.5'$. The lower panel shows the corresponding background values for the 4 profiles.

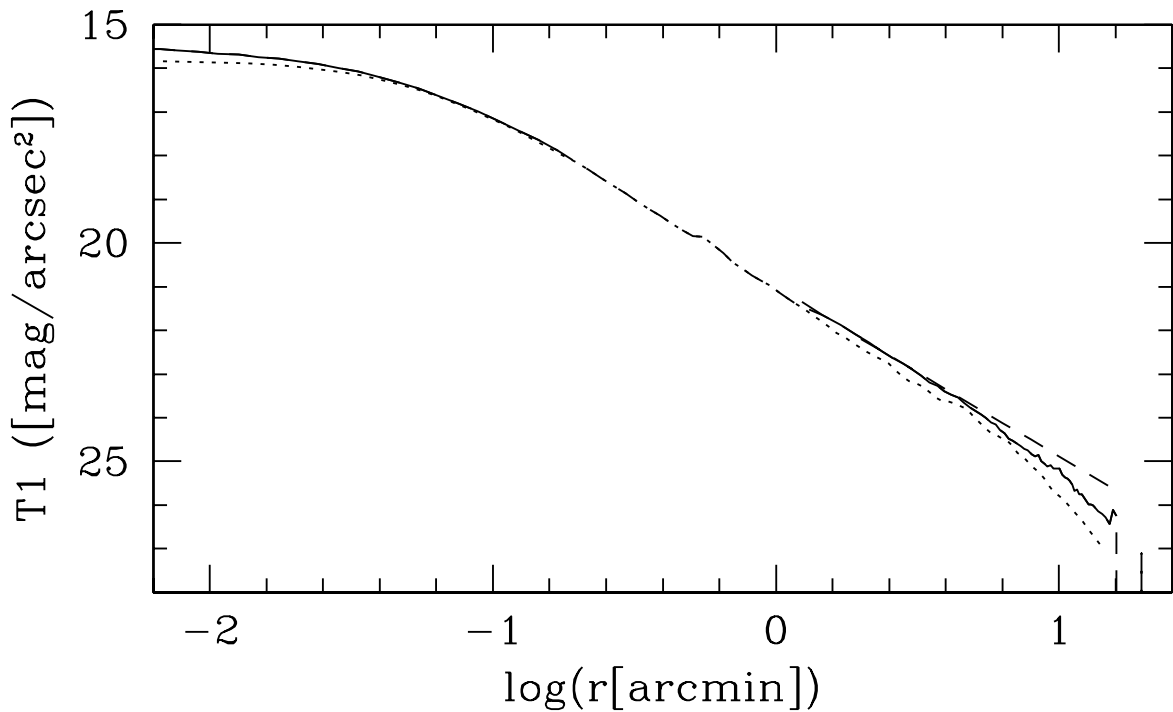


Fig. 15.— The T1-luminosity profile of NGC 1399. We shifted all profiles (even if measured in a different passband) to our profile, which is the solid line at large radii. The profile of Caon et al. ((1994)) is the short dashed curve, the one of Schombert et al. ((1986)) the long dashed curve and the HST profile by Lauer et al. ((1995)) is the solid line at small radii.

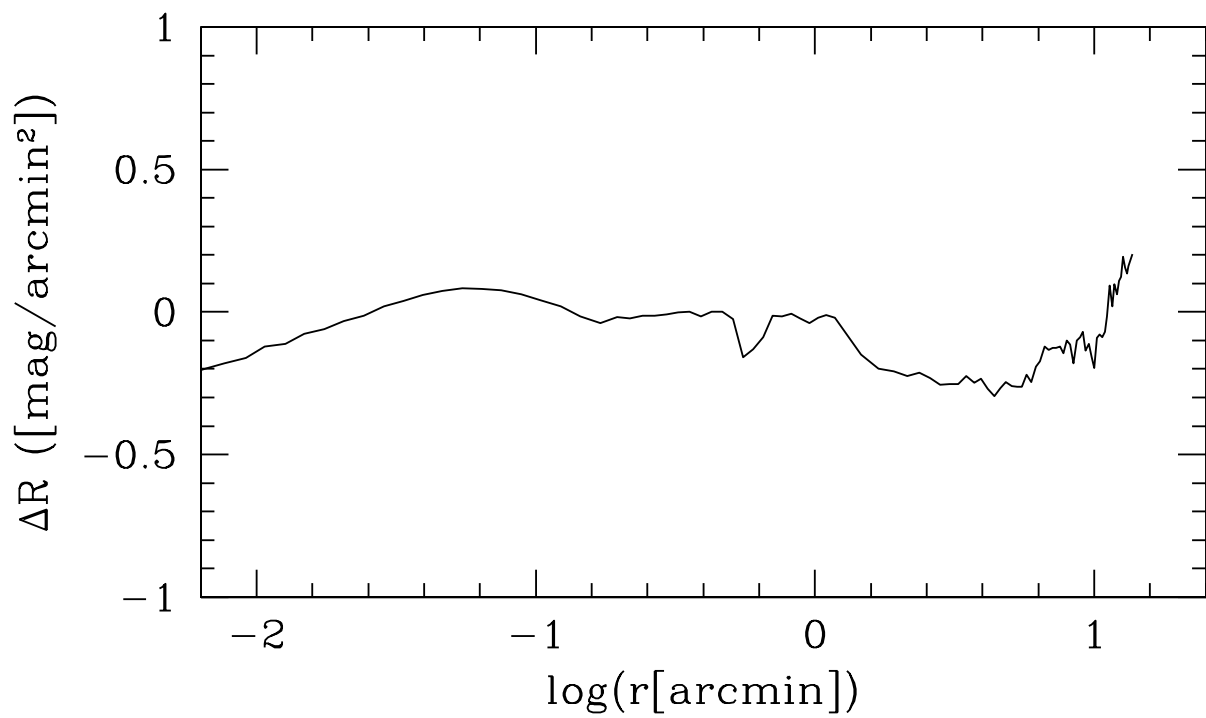


Fig. 16.— Difference between the observed and fitted galaxy light profile. Positive values mean fit values brighter than observed.

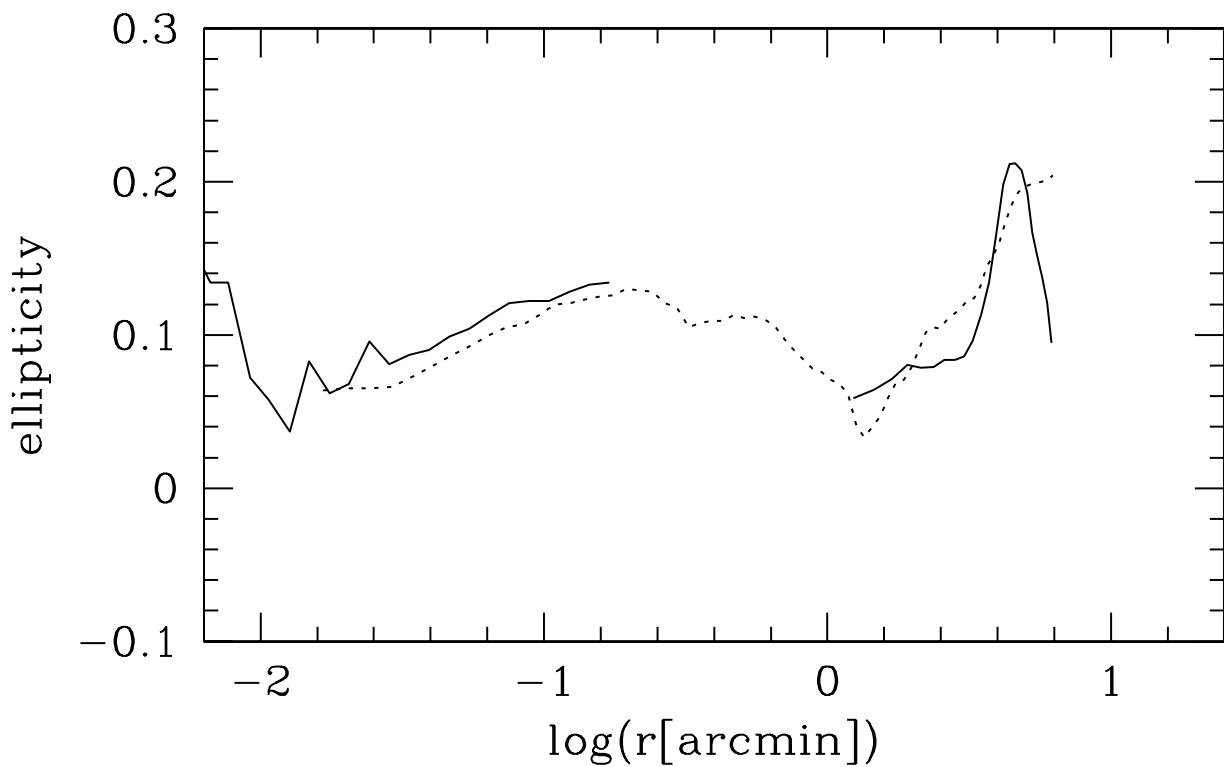


Fig. 17.— The radial dependence of the ellipticity of the galaxy T1 light is plotted as solid lines in the outer region using our MOSAIC data (using a fixed position angle at 90°) and in the inner part using that of Lauer et al. ((1995)). The dashed line shows the ellipticity derived by Caon et al. ((1994)).

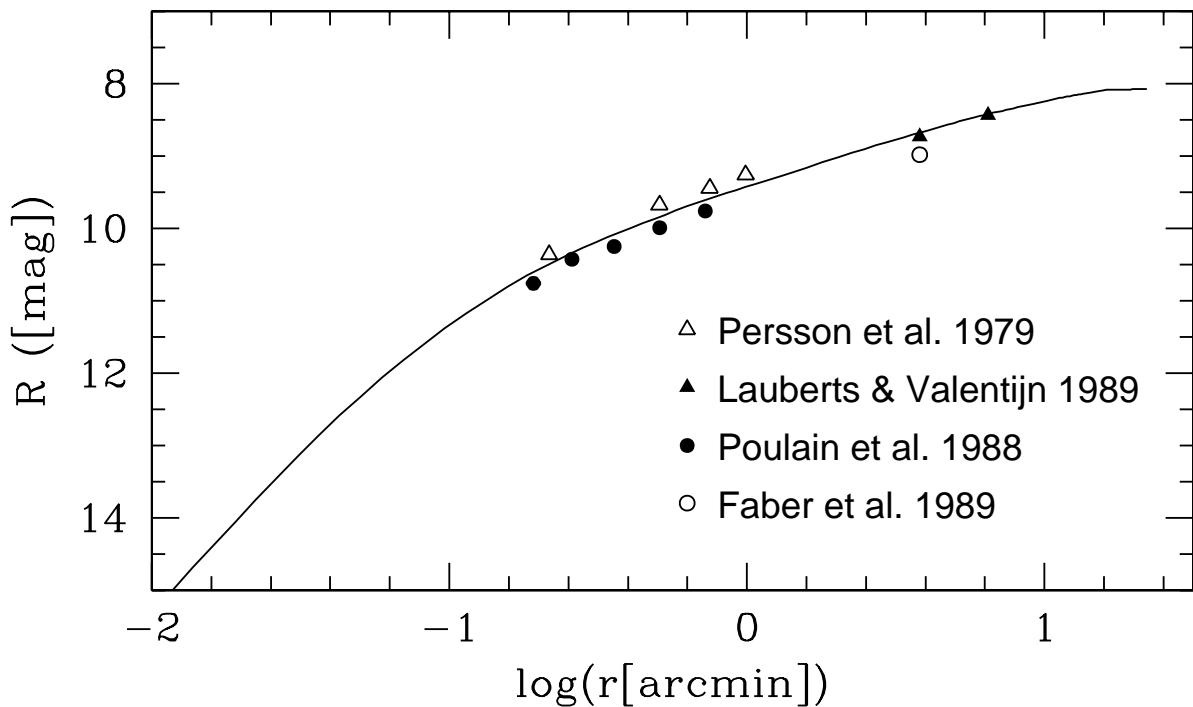


Fig. 18.— Integrated R magnitude dependence on radius for our data and from various literature sources. For this purpos the T1 measurements have been transformed into R measurements.

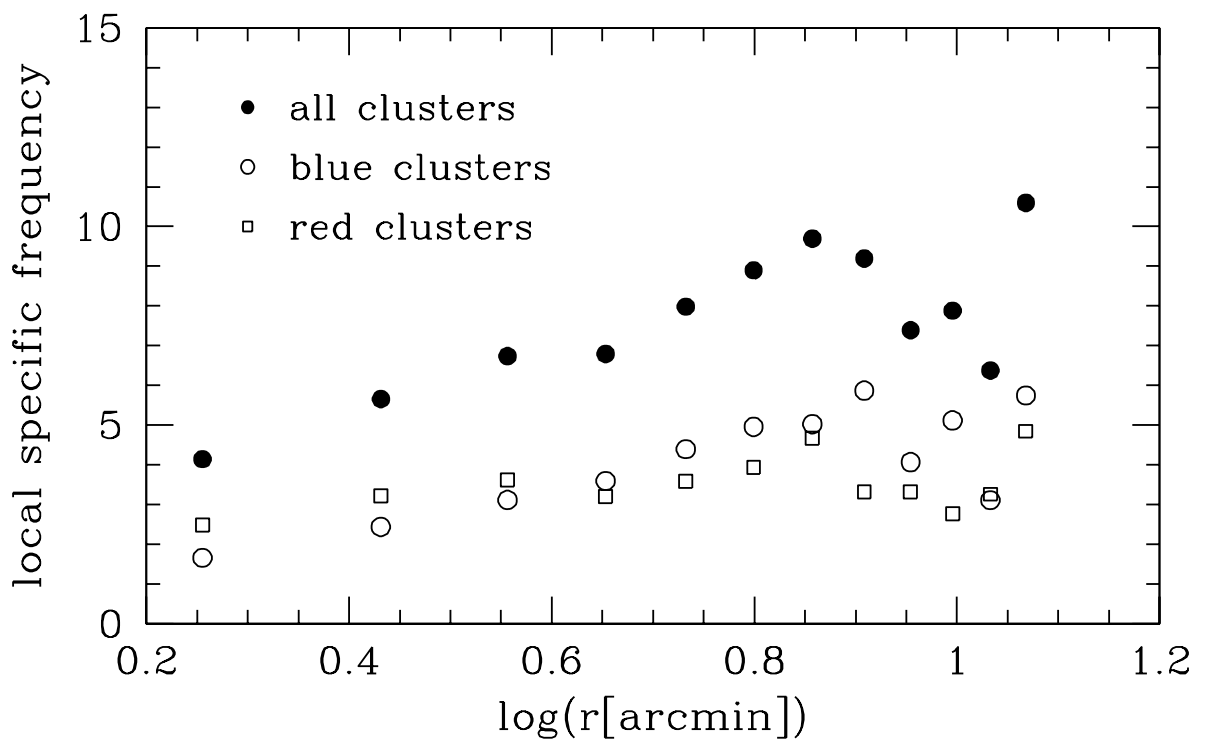


Fig. 19.— The radial local specific frequency is plotted for the whole cluster sample and for the metal-rich and metal-poor subsamples.

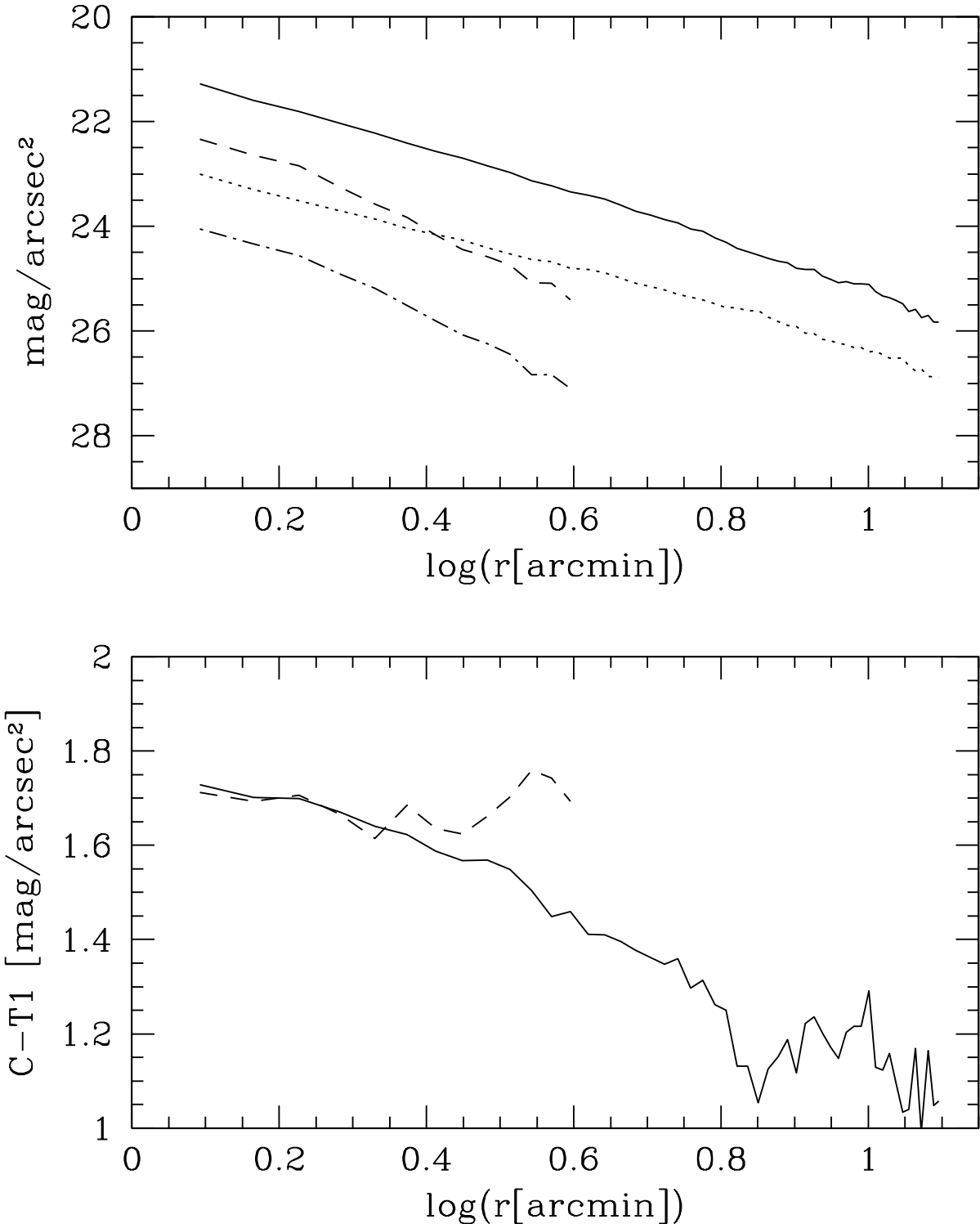


Fig. 20.— **Upper panel:** The luminosity profile in T1 (solid line) and C (dotted line) of NGC 1399 is be compared to the T1 (dashed line) and C (dash-dotted line) surface luminosity of NGC 1404. **Lower panel:** The radial color is plotted for NGC 1399 (solid line) and NGC 1404 (dashed line).

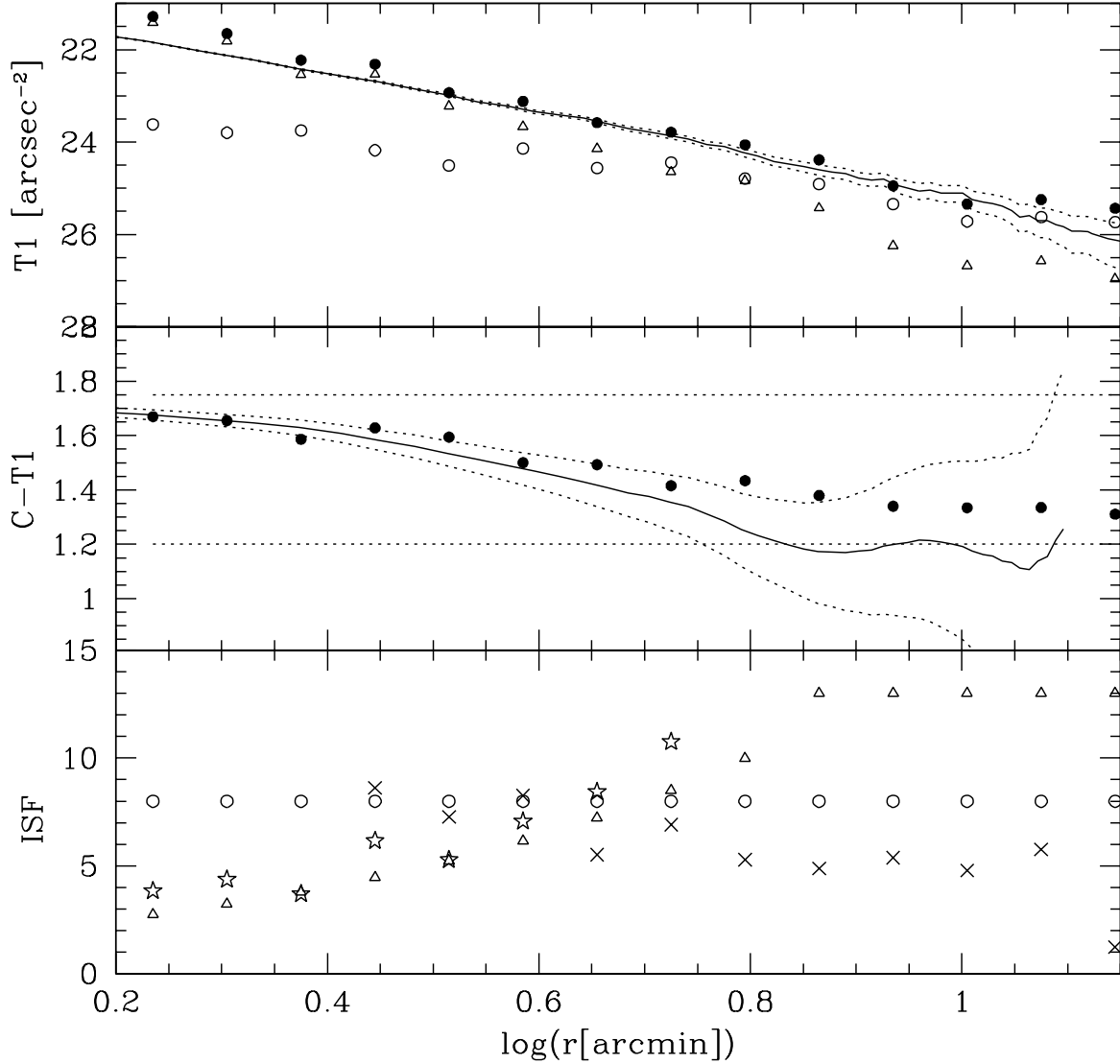


Fig. 21.— A simple model to fit the galaxy light profile measured in the C and R band. In the **upper panel** the galaxy light is shown as solid lines accompanied by estimated errors due to background variations. The solid circles show the model light distribution, that is a composite of the contribution of the red (triangles) and blue (open circles) populations. The two horizontal lines indicate the color that has been used as mean color for the two populations. In the **middle panel** the color profile is plotted with a solid line together with the estimated errors and compared to the model color distribution (solid circles). In the **lowest panel** we plotted as open circle and open triangle the two ISF that define the model for blue and red population respectively. The crosses and the diamonds show the ISF for blue and red populations, respectively, when it is directly calculated.